Nemo-like kinase disrupts nuclear import and drives TDP43 mislocalization in ALS

Michael E. Bekier II[1#], Emile Pinarbasi[1,2#], Jack J. Mesojedec[1], Layla Ghaffari[3], Martina de Majo[3], Erik Ullian[4], Mark Koontz[3], Sarah Coleman[3], Xingli Li[1], Elizabeth M. H. Tank[1], Jacob Waksmacki[1], Sami Barmada[1]*

[1]Department of Neurology, University of Michigan, Ann Arbor, MI, 48109, United States

[2]Department of Pathology, Michigan Medicine, University of Michigan, Ann Arbor, MI, 48109, United States

[3]Synapticure, Chicago, IL, United States 60612

[4]Department of Ophthalmology & Physiology, University of California San Francisco, San Francisco, CA, 94143, United States

# contributed equally

*Correspondence to Sami Barmada: 109 Zina Pitcher Place, Ann Arbor, MI, 48019; 734-764-8425; sbarmada@umich.edu

Conflict of Interest Statement:

S.J.B. serves on the advisory board for Neurocures, Inc., Symbiosis, Eikonizo Therapeutics, 15 Ninesquare Therapeutics, the Live Like Lou Foundation, Synapticure, and the Robert Packard

Center for ALS Research. S.J.B. has received research funding from Denali Therapeutics, Biogen, Inc., Lysoway Therapeutics, Amylyx Therapeutics, Acelot Therapeutics, Meira GTX, Inc., Prevail Therapeutics, Eikonizo Therapeutics, and Ninesquare Therapeutics.

Abstract

Cytoplasmic TDP43 mislocalization and aggregation are pathological hallmarks of amyotrophic lateral sclerosis (ALS). However, the initial cellular insults that lead to TDP43 mislocalization remain unclear. In this study, we demonstrate that Nemo-like kinase (NLK)—a proline-directed serine/threonine kinase—promotes the mislocalization of TDP43 and other RNA-binding proteins by disrupting nuclear import. NLK levels are selectively elevated in neurons exhibiting TDP43 mislocalization in ALS patient tissues, while genetic reduction of *NLK* reduces toxicity in human neuron models of ALS. Our findings suggest that NLK is a promising therapeutic target for neurodegenerative diseases.

33 **Introduction**

34 Amyotrophic lateral sclerosis (ALS) is a fatal and progressive neurodegenerative disease
35 distinguished by loss of motor neurons in the cortex and spinal cord (1). The clinical presentation of
36 ALS is heterogeneous, depending in large part upon the neuroanatomical pathways involved.
37 Despite this, a single pathological hallmark — mislocalization and aggregation of the RNA binding
38 protein TDP43 — is found in >95% of individuals (2).

39 TDP43 is crucial for several aspects of RNA processing, including RNA splicing, stability and
40 transport (3-7). TDP43 is primarily nuclear in healthy cells, in contrast to the nuclear exclusion and
41 cytosolic deposition of TDP43 that are characteristic of ALS (3). Although the origins of TDP43
42 mislocalization are unclear, deficiencies in nucleocytoplasmic transport machinery are
43 increasingly implicated as a potential contributing factor to ALS pathology (8). Impaired nuclear
44 import of TDP43 and other RNA binding proteins, together with dysfunction of the nuclear pore
45 complex itself, are observed in human induced pluripotent stem cell (iPSC)-derived neurons from
46 sporadic and familial ALS patients as well as post-mortem samples. Genetic screens in ALS model
47 systems have repeatedly uncovered nuclear pore and nucleocytoplasmic transport factors as
48 potent disease modifiers, confirming the significance of these pathways in disease pathogenesis
49 (9-11).

50 Among the most consistent and dramatic disease modifiers to emerge from these screens is
51 nemo-like kinase (NLK), a proline directed serine-threonine kinase that regulates cell
52 differentiation (12), proliferation, and apoptosis (13, 14). NLK depletion mitigates disease
53 phenotypes not just in *Drosophila* and murine models of ALS, but also murine models of
54 spinobulbar muscular atrophy, and murine models of spinocerebellar ataxia (15-17). Conversely,

55 NLK overexpression reduces toxicity in Huntington's disease models, indicating context-dependent
56 effects of NLK in neurodegeneration (18).

57 NLK has several predicted substrates that function in nucleocytoplasmic transport, but whether
58 NLK itself may influence nuclear import and ALS pathogenesis remains unknown. Here, we
59 demonstrate that NLK is a pivotal regulator of nucleocytoplasmic transport. NLK accumulation
60 leads directly to the cytoplasmic accumulations of TDP43 and other RNA-binding proteins
61 associated with ALS, while reduction in NLK promotes the survival of iPSC-derived neurons
62 carrying ALS-associated mutations. Importantly, NLK is upregulated selectively in affected neurons
63 from ALS patients and correlates with TDP43 mislocalization, implicating NLK as a key determinant
64 of disease pathophysiology and highlighting NLK as a promising therapeutic target for ALS and
65 related TDP43 proteinopathies.

66

67 **Results**

68 **NLK overexpression drives mislocalization of TDP43 and other ALS-linked RNA-binding**
69 **proteins**

70 To determine if NLK is capable of directly influencing TDP43 localization, we transfected HEK293
71 cells with plasmids encoding FLAG-tagged wild-type (WT) NLK and examined TDP43 localization by
72 immunofluorescence (Figure 1A). Exogenous NLK, like endogenous NLK, is both cytoplasmic and
73 nuclear in distribution (19). As a control, we also transfected cells with plasmids encoding FLAG-
74 tagged kinase-negative (KN) NLK, which harbors a point mutation in the active site (K155M) that
75 abrogates kinase activity (19). NLK WT overexpression significantly decreased the nuclear-
76 cytoplasmic (NC) ratio of endogenous TDP43 compared to NLK KN (Figure 1B). The change in

77 TDP43 NC ratio was driven by both a reduction in nuclear TDP43 as well as a concordant increase
78 in cytoplasmic TDP43, consistent with nuclear-cytoplasmic TDP43 mislocalization (Figure 1C-D).

79 We next asked whether NLK WT solely affected TDP43 localization, or whether it also regulated the
80 distribution of other ALS-associated RNA binding proteins that undergo nucleocytoplasmic
81 transport, including HNRNPA2B1 and Matrin-3. We also examined the localization of FUS, an RNA
82 binding protein harboring a non-classical PY-nuclear localization signal (NLS) recognized by
83 importin-$ß_2$, in contrast to the classical K/R-rich NLS in TDP43, HNRNPA2B1, and MATR3 that binds
84 importin-α (20-22). As before, HEK293 cells were transfected with KN or WT NLK, and the
85 subcellular distribution of each protein determined by immunofluorescence (Figure 1F-K).
86 Compared to NLK KN, NLK WT overexpression significantly reduced the NC ratio of both FUS and
87 HNRNPA2B1 but had no significant effect on Matrin-3 localization (Figure 1F-K). Together, these
88 findings suggest that WT NLK overexpression disrupts nuclear localization of multiple RNA-binding
89 proteins harboring classical as well as non-classical NLSs, in a kinase-dependent manner.

90

91 **NLK overexpression disrupts nuclear import**

92 At steady state, nuclear localization of TDP43 and other RNA-binding proteins is maintained
93 through two competing processes: active nuclear import and passive efflux through the nuclear
94 pore (23-25). To directly evaluate nuclear import, we co-expressed NLK together with YFP fusion
95 proteins containing NLS sequences from TDP43 (YFP-NLS^{TDP}), FUS (YFP-NLS^{FUS}), Matrin-3 (YFP-
96 NLS^{MATR3}) and SV40 (YFP-NLS^{SV40}, a canonical classical NLS) followed by immunofluorescence for
97 TDP43, FUS, or Matrin-3 (Figures 2A-H). Notably, WT NLK expression drives mislocalization of YFP-
98 NLS^{MATR3}, but not endogenous Matrin-3 (Figure 1J, K), potentially due to the relatively large size of
99 Matrin-3 (95kDa, vs 27kDa for YFP-NLS^{MATR3}) (23, 24). Compared to overexpression of NLK KN, NLK

100 WT significantly increased the NC ratio of all NLS-fusion proteins (Figure 2C). Similar to what we
101 observed for native RNA binding proteins (Figure 1), WT NLK affects reporters containing both
102 classical as well as non-classical NLS motifs (26). Collectively, these data indicate that WT NLK
103 overexpression disrupts global nuclear import through its kinase activity.

104

105 **NLK-induced TDP43 mislocalization is independent of KPNA2 nuclear accumulation**

106 Nuclear import relies on transport receptor proteins, such as KPNA2 and KPNB1, which recognize
107 and bind to NLS-containing proteins such as TDP43 (27). Thus, we examined the sub-cellular
108 localization of KPNB1 and KPNA2 by immunofluorescence after overexpression of either KN or WT
109 NLK. Overexpression of WT NLK significantly increased the NC ratio of both KPNA2 and KPNB11,
110 driven by a significant increase in their nuclear fractions without a corresponding decrease in their
111 cytoplasmic abundance (Figure 3A-D, S1A-B). Because of the critical importance of these factors
112 for nuclear import, we questioned whether the mislocalization of TDP43 and other RNA binding
113 proteins may be secondary to the observed nuclear accumulation of KPNA2 and/or KPNB1. To test
114 this hypothesis, we took advantage of previous data showing that nuclear accumulation of KPNA2
115 can be reversed by the expression of the E3 ubiquitin ligase FBXW7 (28). HEK293 cells were
116 transfected with plasmids encoding FLAG-tagged NLK WT and either mApple (negative control) or
117 FBXW7 followed by immunofluorescence for KPNA2 (Figure 3E, F). Compared to mApple, FBXW7-
118 V5 significantly reduced the NC ratio of KPNA2 in NLK-overexpressing cells (Figure 3G), due
119 primarily to reduction in the nuclear KPNA2signal (Figure 3D, S1C). Despite this, FBXW7-V5
120 coexpression failed to significantly correct TDP43 mislocalization in cells transfected with WT NLK
121 (Figure 3G, H, S1D). These results indicate that NLK-induced mislocalization of TDP43 does not
122 depend on the nuclear accumulation of KPNA2.

123

124 **NLK overexpression promotes mislocalization of Ran, Ran-GAP1, and RanBP2**

125 Nuclear localization of receptor-bound cargo is mediated by RanGAP1 and RanBP2, nuclear pore-
126 associated factors that regulate the Ran gradient (29)(Figure S2). Consistent with a previous screen
127 for kinase-interacting proteins (30), both RanGAP1 and RanBP2 co-immunoprecipitated with FLAG-
128 NLK in HEK293 cells (Figure 4A-C). NLK overexpression also promoted the accumulation of non-
129 sumoylated RanGAP1 (Figure 4A). RanGAP1 sumoylation is critical for nuclear envelope
130 localization and its interaction with RanBP2 (Figure 4 C, (31-33)). This prompted us to investigate
131 the impact of NLK overexpression on the subcellular localization of RanGAP1, RanBP2, and
132 ultimately Ran. Compared to KN NLK overexpression, WT NLK significantly disrupted the expected
133 nuclear envelope localization of RanGAP1 and RanBP2 as measured by the ratio of nuclear rim
134 density to cytoplasmic density (Figure 4D-G). Conversely, overexpression of NLK WT did not
135 significantly impact FG nucleoporins as detected by MAb414 (Figure 4H, I). WT NLK overexpression
136 also reduced the NC ratio of Ran, driven by both a decrease in nuclear Ran and an increase in
137 cytoplasmic Ran (Figure 4J, K). As such, NLK-induced disruption of the Ran gradient correlates with
138 disruption of the RanGAP1-RanBP2 complex and impaired nucleocytoplasmic transport.

139

140 **NLK drives redistribution of mRNA and disassembles nuclear speckles**

141 The localization of TDP43 and other RNA-binding proteins is heavily influenced not just by their NLS
142 motifs, but also by their cognate RNA substrates (34). Based on this, we examined whether TDP43
143 mislocalization upon WT NLK overexpression is RNA-dependent. Initially, we transfected HEK293
144 cells with an EGFP-tagged variant of TDP43 harboring two mutations within RRM1 that abolish RNA
145 binding, TDPF2L-EGFP (F147L/F149L)(35, 36) , together with WT or KN NLK (Figure 5A). TDPF2L-

146 EGFP formed phase-separated droplets that were largely restricted to the nucleus in cells co-
147 expressing KN NLK, as in prior studies (37). However, co-transfection with WT NLK resulted in the
148 appearance of cytosolic TDP43F2L-EGFP droplets, suggesting that TDP43 mislocalization upon WT
149 NLK overexpression is independent of RNA binding (Figure 5A and S3A).

150 We also investigated whether WT NLK overexpression could affect the distribution of
151 polyadenylated (polyA) mRNA. We first immunostained for NXF1, an mRNA export factor which
152 itself contains a PY-NLS (20) and saw that in NLK WT transfected cells, NXF1 accumulates in the
153 cytoplasm (Figure 5B and S3B). Next, we directly assessed mRNA distribution using fluorescence
154 in-situ hybridization (FISH). While untransfected and KN NLK-expressing cells displayed a punctate
155 pattern of polyA mRNA within the nucleus, WT NLK overexpression resulted in a more diffuse and
156 evenly distributed nuclear signal, and minimal changes in the polyA mRNA NC ratio (Figure 5C and
157 S4C). Given the enrichment of polyA mRNA within nuclear speckles, and the apparent loss of such
158 structures with WT NLK overexpression, we also immunostained WT or KN NLK-transfected cells
159 using the SC35 antibody, which recognizes SRRM2, a core component of nuclear speckles (38). WT
160 NLK-expressing cells, in contrast to untransfected or KN NLK-transfected cells, displayed a
161 dramatic reduction in nuclear speckles (Figure 5D). This effect appeared to be specific for nuclear
162 speckles, as we saw no change in other nuclear membraneless organelles such as paraspeckles
163 (marked by SFPQ (39); Figure 5E) or nucleoli (marked by nucleophosmin (40); Figure 5F) in WT NLK-
164 expressing cells.

165

166 **NLK overexpression disrupts nuclear import in mammalian neurons**

167 To examine the impact of NLK overexpression on RBPs and nuclear import factors in neurons, we
168 transfected rodent primary mixed cortical neurons with either SNAP-FLAG (SF; negative control) or

169 SNAP-FLAG-NLK WT (SF-NLK) before immunostaining for TDP43 and other factors affected by NLK.
170 Consistent with our results in HEK293 cells, expression of SF-NLK but not SF significantly impacted
171 the subcellular localization of TDP43, FUS, RanGAP1, RanBP2, and Ran (Figure 6A-D). As before,
172 the central channel of the NPC marked by FG nucleoporins was unaffected by SF-NLK expression
173 (Figure 6E), while exogenous reporters such as YFP-NLS^{SV40} were mislocalized by SF-NLK but not SF
174 in transfected neurons (Figure S4).

175 Nucleocytoplasmic trafficking is essential for maintaining protein and RNA homeostasis; thus, we
176 predicted that NLK-induced disruption of nucleocytoplasmic transport would lead to substantial
177 toxicity. To assess this, we utilized automated longitudinal microscopy to track hundreds of rodent
178 primary mixed cortical neurons cultures prospectively for 10 days in culture. Neurons were
179 transfected with SF or SF-NLK, in combination with a survival marker (GFP) enabling us to
180 determine the time of cell death (Figure 6F, G). SF-NLK overexpression significantly increased the
181 cumulative risk of death in transfected neurons compared to SF alone (HR=1.61, $p<0.001$, Cox
182 proportional hazards analysis; Figure 6H). Since all data on survival are acquired from individual
183 neurons, and the abundance of fluorescently-tagged proteins is directly proportional to the
184 measured signal intensity (41), we investigated the relationship between SNAP-FLAG-NLK intensity
185 and the hazard of the event using a Cox proportional hazards model with penalized splines (42-44).
186 The Cox model revealed significant non-linear relationships between signal intensity and hazard,
187 as indicated by a Likelihood Ratio Test statistic of χ^2 (4.06) = 25.89 ($p < 0.0001$), suggesting that the
188 model fits the data well. The concordance index was 0.587, indicating a moderate ability of the
189 model to discriminate between different hazard levels. Hazard ratios were calculated for distinct
190 intensity segments derived from the spline model. For low signal intensities, the hazard ratio was
191 0.898 (95% CI: 0.378 - 2.132), indicating a slight decrease in hazard compared to the baseline. In
192 the medium intensity range, the hazard ratio increased to 1.555 (95% CI: 0.532 - 4.545), suggesting

193 a potential increase in risk. Notably, for high signal intensities, the hazard ratio rose significantly to
194 4.629 (95% CI: 0.701 - 30.584), reflecting a substantial elevation in hazard associated with
195 increased signal intensity (Figure 6I). Collectively, our data indicate that overexpression of NLK
196 significantly impairs the mechanisms that regulate nucleocytoplasmic transport, leading to the
197 mislocalization of pertinent RNA-binding proteins and ultimately neuron death.

198

199 **Increased NLK levels correlate with TDP43 pathology in disease models and patients**

200 Approximately 50% of individuals with frontotemporal lobar degeneration (FTLD) show TDP43
201 mislocalization as in ALS(3). In addition, up to half of people with ALS demonstrate cognitive
202 impairment reminiscent of FTLD, while ~1/3 of those with FTLD show motor neuron disease that is
203 indistinguishable from ALS (3, 45). These observations, as well as shared genetics underlying both
204 ALS and FTD, testify to the close overlap between ALS and FTLD with TDP43 pathology (FTLD-TDP)
205 (3, 45). Therefore, to determine if NLK dysregulation may be involved in ALS/FTLD-TDP disease
206 pathogenesis, we initially investigated *NLK* expression in *GRN* knockout mature brain organoids
207 (mbOrgs), an FTLD-TDP model that recapitulates key pathological features of disease, including
208 TDP43 mislocalization, phosphorylated TDP43, and characteristic missplicing of TDP43 substrate
209 RNAs (46). Neurogenin-2 inducible cortical neurons (iNeurons) and mature cortical astrocytes
210 (iAstrocytes) derived from isogenic wild-type (WT) or GRN-/- iPSCs were combined in fixed ratios to
211 form mbOrgs (Figure 7A). RNA-seq revealed significantly elevated normalized counts of *NLK* in
212 GRN-/- mbOrgs compared to WT controls (Figure 7B), a finding that was also confirmed by
213 quantitative RT-PCR (qRT-PCR) (Figure 7C).

214 To further explore the link between NLK changes and TDP43 pathology, we turned to a unique
215 dataset generated by Liu et al. in which neuronal nuclei were sorted from frontal cortices of FTLD-

216 TDP patients into two populations — those with and without nuclear TDP43 – prior to RNA
217 sequencing (RNA-seq) (30). Reanalysis of these data demonstrated a significant upregulation of
218 *NLK* mRNA in nuclei lacking TDP43 (Figure 7D). Using dual-immunohistochemistry, we confirmed
219 that spinal neurons from ALS spinal cord sections with TDP43 pathology (nuclear loss of TDP43
220 with cytosolic inclusions) exhibited more intense staining for NLK in comparison to unaffected
221 neurons present in the same section (Figure 7E and S5C). Dual staining for NLK and TDP43 was
222 also performed in sections from four control patients without spinal pathology (Figure S5D5),
223 showing no clear differences in NLK abundance. These results demonstrate a clear relationship
224 between elevated NLK, at both the mRNA and protein levels, and TDP43 mislocalization in FTLD-
225 TDP and ALS.

226 Together, these data show that NLK is upregulated in human patients and in disease models
227 featuring TDP43 pathology, in accord with our data demonstrating TDP43 mislocalization upon NLK
228 overexpression.

229

230 **NLK reduction improves survival in iPSC-derived neuron models of ALS**

231 Given the detrimental effects of NLK overexpression on nucleocytoplasmic transport (Figures 1-6)
232 and neuron survival (Figure 6), and the elevated *NLK* mRNA and protein observed in patients and
233 disease models (Figure 7A-E), we asked whether targeting *NLK* could ameliorate disease
234 phenotypes in ALS/FTLD-TDP models. First, we examined the survival of iPSC-derived neurons
235 carrying *C9ORF72* expansions, the most prevalent mutation underlying familial ALS and FTLD-TDP
236 in Europe and North America (47, 48). Non-disease and *C9ORF72* mutant neurons were
237 transduced with virus encoding non-targeting or *NLK* shRNA, resulting in a ~50% reduction in NLK
238 RNA levels compared to non-targeting shRNA (Figure 7F). Individual neurons were followed by

239 automated microscopy for 10 days, as before (Figure 7G), and differences in survival assessed via
240 Cox proportional hazards analysis. Three separate lines of *C9ORF72* mutant neurons exhibited
241 significantly higher cumulative risks of death compared to unrelated non-disease neurons (Figure
242 7H and S6A-C). Transduction with *NLK* shRNA significantly reduced the cumulative risk of death in
243 all three lines of *C9ORF72* neurons (HR= 0.403, p= 7.71e-50). To examine if NLK reduction is
244 neuroprotective outside of *C9ORF72* mutations, we utilized an isogenic pair of *TARDBP* mutant
245 iPSC-derived neurons that were created by CRISPR/Cas9 genome engineering (49). In comparison
246 to isogenic controls ("WT"), *TARDBP* mutant (M337V) neurons transduced with lentivirus
247 expressing non-targeting shRNA exhibited a significantly higher cumulative risk of death (Figure 7I).
248 As with *C9ORF72* mutant neurons, however, transduction with *NLK* shRNA-expressing virus
249 significantly extended the survival of M337V neurons (HR = 0.227, p= 0.0013). Collectively, these
250 data imply that *NLK* overexpression is toxic, while *NLK* reduction promotes neuronal survival in
251 models of ALS and FTLD-TDP.

252

253 **Discussion**

254 Our findings indicate that NLK overexpression disrupts the nuclear import and localization of
255 TDP43 and related RNA-binding proteins, including FUS and HNRNPA2B1, in a kinase-dependent
256 manner. These effects correlate with the mislocalization of the RanBP2-RanGAP1 complex and
257 collapse of the Ran gradient, both of which are crucial for functional nucleocytoplasmic transport.
258 As expected based on these observations, NLK dose-dependently increased the risk of death in
259 primary rodent neurons. Notably, we uncovered elevated NLK expression selectively in neurons
260 with TDP-43 pathology both at the RNA level (in FTLD-TDP frontal cortex) and at the protein level (in
261 ALS spinal cord). NLK was also upregulated in a brain organoid model of FTLD-TDP, while reducing

262 NLK in human iPSC-derived neurons carrying disease-associated mutations prolonged survival.
263 These results suggest that NLK may contribute to the pathology of ALS-FTLD-TDP by impairing
264 nucleocytoplasmic transport and promoting neurotoxicity. Targeting NLK protein levels or kinase
265 activity could thus represent a novel therapeutic approach for ALS, FTLD-TDP and other TDP43
266 proteinopathies.

267 Disruption of the Ran gradient, mislocalization of nuclear pore components, and disturbance of
268 nuclear pore architecture — all of which we observed upon NLK overexpression — have likewise
269 been described in ALS/FTLD-TDP samples and disease models (9-11, 50). There is no predicted
270 NLK phosphorylation site within TDP43 itself; rather, we suspect that NLK may interfere with the
271 nucleocytoplasmic transport of several RNA binding proteins and other factors by acting on
272 integral components of the nuclear pore. We and others noted a direct interaction between NLK
273 and the RanGAP1-RanBP2 complex ((30); see Figure 4), which is critical for maintaining the Ran
274 gradient and nuclear import/export (51). NLK overexpression prevented RanGAP1 sumoylation
275 (Figure 4A) and reduced the amount of RanGAP1 in complex with RanBP2 (Figure 4C). In the
276 absence of sumoylation, RanGAP1 is unable to bind RanBP2 or localize to the nuclear envelope
277 (Figure 4C, (31-33). One possibility is that NLK directly phosphorylates RanGAP1, inhibiting its GAP
278 activity (50) as well as its sumoylation, thereby disrupting its interaction with RanBP2 at the nuclear
279 pore complex. Alternatively, NLK may negatively regulate Ubc9, a SUMO E3 ligase required for
280 recruitment of RanGAP1 to the RanBP2 complex. None of these possibilities are mutually
281 exclusive; NLK may impact nucleocytoplasmic transport through more than one overlapping
282 mechanism.

283 At baseline, NLK is highly expressed in the CNS, and its expression is unregulated by oxidative and
284 osmotic stress (52, 53), conditions associated with the cytosolic accumulation of TDP43 and other,
285 predominantly nuclear, RNA binding proteins. NLK interacts with several proteins associated with

286 neurodegenerative diseases, including poly-Q expanded androgen receptor in spinobulbar
287 muscular atrophy (SBMA) and ataxin-1 in spinocerebellar ataxia 1 (SCA1) (16, 17); accumulations
288 of these proteins may also contribute to changes in NLK expression and/or activity. Although
289 previous studies have failed to detect NLK upregulation in disease, in most cases these
290 investigations are limited to evaluation of NLK levels (RNA or protein) in bulk tissue. In contrast, our
291 work revealed NLK upregulation solely within affected neurons displaying TDP43 pathology, in
292 association with evidence of disrupted nucleocytoplasmic trafficking in the same cells, suggesting
293 that NLK expression changes are restricted to cells with TDP43 redistribution. Outside of changes
294 in expression, NLK may also be inappropriately activated in disease via diverse stimuli.
295 Proinflammatory factors such as transforming growth factor ß (TGFß), interleukin-6 (IL6) and Wnt
296 all activate NLK through MAPK-dependent signaling (54). Notably, TGF-ß is upregulated in ALS (55),
297 and aberrant Wnt signaling is associated with TDP43 mislocalization in cellular and animal models
298 (56).

299 NLK is an essential kinase — homozygous *Nlk* deletion results in death *in utero* or postnatally,
300 depending on the mouse strain (57, 58). Conditional *Nlk* knockout in adult animals is well-
301 tolerated, however (59), and *Nlk* haploinsufficiency (*Nlk*+/-) is protective in several
302 neurodegenerative disease models, including TDP43-overexpressing mice (15-18). Similarly, partial
303 *NLK* knockdown in our investigations was associated with extended survival in *C9ORF72* and
304 *TARDBP* mutant human iPSC-derived neurons and was safe in control neurons. These data indicate
305 that even modest reductions in *NLK* may be sufficient for mitigating neurodegeneration in ALS and
306 FTLD-TDP.

307 Although prior interaction studies highlighted several potential partners for NLK, its substrates in
308 neurons and phosphorylation sites within these substrates remain largely unexplored. RanBP2 and
309 RanGAP1 are two potential targets for NLK with clear connections to nucleocytoplasmic transport,

310 but NLK is also likely to act on distinct substrates and disease-related pathways, including the
311 integrated stress response and autophagy (15). One advantage of therapeutic strategies that act on
312 upstream signaling factors such as NLK is the capacity to influence several neuroprotective
313 mechanisms simultaneously. Nevertheless, not all downstream events are likely to be
314 beneficial(18), emphasizing the need for further investigations into NLK targets and the impact of
315 NLK-mediated phosphorylation on their function and contribution to disease.

316

317

318 **Methods**

319 **Sex as a biologic variable**

320 Our study examined tissue from both male and female patients, and similar findings are reported
321 for both sexes.

322

323 **HEK293 cell culture and transfection**

324 Human embryonic kidney (HEK) 293T were cultured in DMEM (Gibco, 11995065) supplemented
325 with 10% FBS (Gibco, ILT10082147) at 37°C in 5% CO2. Cells were transfected with Lipofectamine
326 2000 (Invitrogen, 11668027) according to the manufacturer's instructions. For experiments with
327 YFP-NLS reporters, the lipofectamine solution was divided toto ensure there would be both cells
328 co-transfected with NLK and reporter as well as cells transfected with the reporter alone. Of the
329 lipofectamine solution, 75% contained two plasmids (NLK and reporter) while the remaining 25%
330 contained reporter alone. The lipofectamine solution was then combined and briefly mixed before
331 adding directly to cells. After 24 hours, transfected cells were split in media containing poly D-

332 lysine (1:500, cat Millipore A-008-E) onto coverslips coated with laminin (1:100, Sigma L2020-
333 1MG). Cells were cultured an additional 24 hours then immunocytochemistry was performed as
334 detailed below.

335

336 **Primary neuron cell culture and transfection**

337 Cortices from embryonic day (E)19-20 Long-Evans rat embryos were dissected and disassociated,
338 and primary neurons were plated at a density of $6x10^5$ cells/mL in 96-well plates or in 24 well plate
339 on coverslips. At *in vitro* day (DIV) 4, neurons were transfected using Lipofectamine 2000 as
340 previously described (49, 60). For experiments with the YFP-NLS reporter, the transfection mix was
341 split as described above for HEK cells. Following transfection, cells were placed in Neurobasal
342 Complete Media (Neurobasal (Gibco 21103-049), 1x B27 Supplement (Gibco, 17504-044), 1x
343 Glutamax, 100 units/mL Pen Strep). Cells were fixed for immunocytochemistry 48 hours after
344 transfection.

345

346

347 **iPSC maintenance and differentiation**

348 Creating Neural Progenitors: iPSCs were dissociated using Accutase, counted, and plated at
349 32,000 cells/mL in E8 media with ROCK inhibitor. Differentiation was then induced with
350 doxycycline for 48 hours (2 µg/mL; Sigma, #D3447). Differentiating neural progenitors (NP) were
351 dissociated using Accutase after two days of doxycycline induction and frozen for future
352 experiments.

353 Differentiating Neural Progenitors: Previously frozen neural progenitors were thawed in E8 media
354 with ROCK inhibitor and incubated for 24 hours. Subsequently, the media was changed to N2
355 media containing 1x N2 Supplement (Gibco, #17502-048), 1x NEAA Supplement (Gibco, #11140-
356 050), 10 ng/mL BDNF (Peprotech, #450-02), 10 ng/mL NT3 (Peprotech, #450-03), 0.2 µg/mL
357 Laminin (Sigma, #L2020), and 2 µg/mL doxycycline (Sigma, #D3447). On Day 2, the media was
358 replaced with transition media (1:1 full E8 media and DMEM/F12 (Gibco, #11320-033)). On Day 3,
359 the media was switched to B27 media, prepared with 1x B27 Supplement (Gibco, #17504-044), 1x
360 Glutamax Supplement (Gibco, #35050-061), 10 ng/mL BDNF, 10 ng/mL NT3, 0.2 µg/mL Laminin, 1x
361 CultureOne (Gibco, #A33202-01), and Neurobasal-A (Gibco, #12349-015). On Day 6, cells were
362 transduced with the virus (University of Michigan Vector Core) and maintained in the same media
363 for the remainder of the experiment.

364

365 **iPSC cell lines**

366 The cell lines 1021 and 793 (controls) and 883 and 321 (C9ORF) were generated and characterized
367 as previously described (7).. The CS52i and corrected cell lines were obtained from Cedars Sinai.
368 See table in Supplementary Methods for additional details.

369 **mbOrg generation**

370 Isogenic human iPSC line WTC11 (GRN+/+ and GRN−/−) were generated by Dr. Bruce R. Conklin, as
371 previously described (61). iPSCs were cultured and maintained in StemMACS™ iPS-Brew XF
372 (Miltenyi Biotec, 130-104-368) media on 6-well cell culture plates (GenClone, 25-105MP) coated
373 with Vitronectin (Gibco, A14700) in DPBS. iPSCs were dissociated and passaged using EDTA
374 (Invitrogen, AM9260G) in DPBS.

375 iA and iN were differentiated separately, plated in a 1:1 ratio, and aged for 4 weeks as previously
376 described (46). For iN differentiation, iPSCs were transduced with NGN2-expressing lentivirus
377 constructs and a previously published protocol was followed for differentiation (61). Briefly, iPSCs
378 are expanded, dissociated, and replated on Matrigel-coated plates. Cells are grown in specialized
379 iNeuron induction media (DMEM-F12 + Glutamax; Gibco, 10565-018), N-2 supplement (Gibco,
380 17502-048), MEM-NEAA (Gibco, 11140-050) containing doxycycline (Sigma, D3072) for 72 h, with
381 media changed every 24 h. Cells are then dissociated using Accutase and plated together with iA.
382 Cortical-like iA are generated as previously described (62). Human induced pluripotent stem cells
383 (GRN+/+ and GRN-/-) were grown on vitronectin coated tissue culture plates using StemMACS™
384 iPS-Brew XF (Miltenyi Biotec, 130-104-368) media. On day 0 of differentiation, iPSCs are
385 dissociated into small aggregates and transferred in neurosphere induction medium (NSIM)
386 (DMEM-F12/Neurobasal-A at 1:1) plus SMAD inhibitors SB431542 and DMH1. On day 7, spheroids
387 are transferred to Matrigel-coated tissue culture plates with NIM. On day 14, rosette clusters were
388 mechanically removed and transferred to tissue culture flasks with NIM plus FGFb (Peprotech,
389 100-18B). Media was changed every 72 hours. On day 20, spheroids were triturated into a single
390 cell suspension and transferred to a new untreated cell culture flask with astrocyte media (ASM)
391 [(DMEM-F12 (Gibco, 10565-018), N2 Supplement (Gibco, 17502-048), B27 -Vit.A Supplement
392 (Gibco, 12587-010), Heparin (Stemcell Tech, 07980)) plus Y27632 (Tocris, 1254)]. From Day 28 to
393 180, spheroid aggregates were maintained in suspension with ASM plus EGF and FGFb (Peprotech,
394 100-15 & 100-18B) with media changes every 4-5 days. Spheroid aggregates were triturated every
395 7-10 days and transferred to new untreated tissue culture flasks. Spheroids are triturated every 7–
396 10 days and transferred to new tissue culture flasks. In order to generate mbOrgs, iN and iA are
397 plated together at a 1:1 ratio on Matrigel-coated 24-well plates at a collective density of ~1x106
398 cells/well. Cells are maintained in BrainPhys Complete medium with a 50% medium change every

399 72 h. mbOrgs will be created on 384-microwell plates as described previously (46), resulting in
400 mbOrgs that are highly uniform in size (~500 m) after brief spin-down and 1–2 days of subsequent
401 culture. These 3D co-cultures were aged for 4 weeks.

402

403 **Longitudinal microscopy**

404 At in vitro day (DIV) 4, neurons were transfected with 100ng of a control fluorescent plasmid to
405 mark cell bodies and 100ng of an experimental construct using Lipofectamine 2000 as previously
406 described (43, 49, 62). Neurons were imaged as described previously (43, 49, 60, 63) using a Nikon
407 Eclipse Ti inverted microscope with PerfectFocus3a 20X objective lens and either an Andor iXon3
408 897 EMCCD camera or Andor Zyla 4.2 (+)sCMOS camera. A Lambda CL Xenon lamp (Sutter) with 5
409 mm liquid light guide (Sutter)was used to illuminate samples, and custom scripts written in
410 Beanshell for use in micromanager controlled all stage movements, shutters, and filters. For
411 automated analyses of primary neuron survival, custom ImageJ/FIJI macros and Python scripts
412 were used to identify neurons and draw cellular regions of interest (ROIs) based upon size,
413 morphology, and fluorescence intensity. Custom Python scripts were used to track ROIs over time,
414 and cell death marked a set of criteria that include rounding of the soma, loss of fluorescence and
415 degeneration of neuritic processes (63, 64). For iNeuron survival, brightfield and fluorescent
416 images for survival experiments started on Day 14 and continued for 10 days. For manual analysis
417 of iNeuron survival, image time-series were processed by flat-field correction and image
418 registration, followed by programmatic de identification for blinded analysis. Time-series images
419 were uploaded to a browser-based server where a trained user manually counted survival using the
420 point tracking mode. GFP-positive cells were identified at T1, and cell fate was tracked in brightfield
421 images, where neuron death (uncensored event) was recorded at the appropriate time point. Living

422 neurons at the final time point were considered right-censored. Cox proportional hazards model
423 was applied to the datasets, stratifying by biological replicates, and the corresponding hazard plots
424 were generated in R.

425

426 **Immunocytochemistry**

427 Cells were fixed with 4% paraformaldehyde (PFA; Sigma, P6148) for 10m, rinsed with PBS, and
428 permeabilized with 0.1% Triton X-100 (Bio-rad, 161-0407) for 10m. Cells were then blocked in 3%
429 bovine serum albumin (BSA; Fisher, BP9703-100) in PBS at RT for 1h before incubation O/N at 4°C
430 in primary antibody diluted in 3% BSA (See table in Supplementary Methods for additional details).
431 Cells were then washed 3 times in PBS and incubated at RT with secondary antibodies diluted
432 1:250 in 3% BSA for 1h. Following 3 washes in PBS containing 1:10,000 Hoechst 33258 dye
433 (Invitrogen, H3569), cells were mounted on Superfrost Plus Microscope Slides (Fisher, 1255015)
434 with Prolong Gold Antifade Mounting Reagent (Fisher, P10144) and imaged as described below.
435 Images were analyzed by collecting measurements within cellular regions of interest using custom
436 ImageJ/FIJI macros. Graphs were made using R.

437

438 **Fluorescence in situ hybridization**

439 Cells were fixed with 4% paraformaldehyde (Cat #) for 10 m, rinsed with PBS and permeabilized
440 with 0.1% Triton X-100 (Bio-rad, 161-0407) for 10m. Cells were then washed with 2X SSC (2 x 5 m)
441 and incubated in hybridization buffer for 2 hours at 37 degrees (8.75% dextran, 1.75X SSC, 17.5%
442 formamide, 0.5 ug/ul yeast tRNA, 10 mmol RVC, 0.1% BSA, 0.002 ug/ul Cy3-oligo (dT) 30 probe).
443 Cells were then washed with successive SSC rinses (4X SSC 15 m, 2X SSC 15 m, 2X SSC 15m).

444 Then immunocytochemistry was performed as above, beginning with blocking in 3% BSA. All
445 solutions prior to hybridization were DEPC treated.

446

447 **Immunohistochemistry**

448 Duplex immunohistochemistry was performed on a Ventana Discovery Ultra stainer (Indianapolis,
449 IN). Slides were dewaxed, rehydrated and subjected to heat induced epitope retrieval on board the
450 stainer. Slides were then subjected to sequential incubation with NLK (Rabbit polyclonal antibody,
451 AbCam, Cambridge, MA, Ab26050, 1:250, 32 minutes) and polymer goat anti-rabbit IgG conjugated
452 to HRP (Ventana) and developed with Discovery Green chromogen (Ventana). After an additional
453 round of heat induced epitope retrieval to remove the NLK primary antibody-secondary antibody
454 complex, the slides were stained with TDP43 (Rabbit polyclonal antibody, Proteintech, Rosemont,
455 IL, 10782-2-AP, 1:2000, 20 minutes), polymer goat anti-rabbit IgG conjugated to HRP and
456 developed with Discovery Brown chromogen (Ventana). Slides were then countered stained with
457 hematoxylin and coverslipped.

458

459 **RNA isolation for bulk RNAseq and RT-PCR**

460 RNA extraction was performed using the Trizol/phenol-Chloroform method (Sigma, T9424) as
461 previously described (62) and according to manufacturer specifications. Each sample contained
462 ~60 mbOrgs, totaling ~3 x10^6 of cells per sample. The extracted RNA was used as a template for the
463 synthesis of complementary DNA (cDNA) through reverse transcription, using iScript™ cDNA
464 Synthesis Kit (Bio-Rad Cat#1708891) according to the manufacturer's protocol.

465

466 **Quantitative PCR**

467 cDNA samples were treated for genomic DNA contamination using DNA-*free*™ DNA Removal Kit
468 (Invitrogen Cat#AM1906) per manufacturer's instructions. The cDNA was then diluted to a
469 concentration of 5 ng/µl and 4 µl of each sample (total of 20 ng) were aliquoted in a MicroAmp™
470 Optical 96-Well Reaction Plate (Thermo Scientific Cat#N8010560) in technical duplicates. Samples
471 were processed using 2X SYBR Green qPCR Master Mix Assay and quantitative PCR was run on
472 QuantStudio 6 Real-Time PCR system following manufacturer's instructions. Data analysis was
473 carried out applying the Pfaffl mathematical model for relative transcript quantification (65) using
474 GAPDH as a housekeeping gene. See table in Supplementary Methods for primer details.
475

476 **RNA Sequencing**

477 RNA sequencing and analysis of RNA integrity was analyzed on an Agilent 2100 Bioanalyzer using
478 RNA 6000 Nano kit (Agilent, 5067-1511). Only samples with an RNA integrity number (RIN) ≥ 9.4
479 were used to perform bulk RNA sequencing. Nugen Universal Plus (Tecan) was used as a library kit
480 and libraries were sequenced on a SP300 flow cell of the Illumina NovaSeq 6000 machine with a
481 paired end 150 bp sequencing strategy (average depth 90 million reads/sample) at UCSF Genomics
482 Core Facility. Genome was aligned to Ensembl Human.GRCh38.103. Kallisto 0.46.01 was used to
483 generate transcript abundance files for each sample. Transcript counts files for each sample were
484 generated using txImport and transcript differential analysis was performed using DESeq2 v1.24.0.
485 A total of 6 samples were spread across two conditions.
486

487 **Confocal microscopy**

488 Confocal images were taken on a Nikon AXR NSPARC confocal system with a 60x NA1.42 Oil/DIS
489 PLan-Apochromat Lambda D objective with a working distance of 1.5 mm, and a 40x CFI
490 Apochromat LWD Lambda S objective with a working distance of 0.30 mm.

491

492 **Light microscopy**

493 Whole-slide images were generated by the University of Michigan Digital Pathology group within the
494 Department of Pathology using an Aperio AT2 scanner (Leica Biosystems) equipped with a 20x NA
495 0.75 Plan Apochromat objective. 40x scanning is achieved using a 2x optical magnification
496 changer. Resolution is 0.25 µm/pixel for 40x scans. Focus during the scan was maintained using a
497 triangulated focus map built from individual focus points determined in a separate step before
498 scanning was started. Proprietary software was used for image processing during the acquisition.
499 TIFs were taken of the entire ventral horn of all cases, then a pathologist selected each neuron,
500 manually drew an ROI, and annotated the TDP status (pathology or no pathology) using custom Fiji
501 scripts. Then deconvolution and analysis were performed using custom Fiji scripts.

502 High quality images for figures were acquired on an Olympus BX51 light microscope equipped with
503 a UPlanSApo100x oil objective with a numerical aperture of 1.40 and a working distance of 0.12
504 mm. Image deconvolution was performed using Fiji.

505 FLAG-NLK-WT and FLAG-NLK KN were a gift from T Ishitani . SNAP-FLAG and SNAP-FLAG NLK were
506 synthesized and subcloned into FUGW. All YFP reporter plasmids were derived from EYFP2-
507 SV40NLS-NES, a kind gift from Yuh Min Chook (67). Site-directed mutagenesis was used to add a
508 stop codon after the SV40NLS. The NLS of TDP43 (residues 82-98) and FUS (residues 495-526)
509 were PCR amplified using primers below, digested with XbaI and BglII, and cloned into the
510 corresponding sites in EYFP2-SV40NLS-NES. The NLS of MATR3 (residues 583-602) was purchased

511 as a Geneblock from Integrated DNA Technologies (IDT), and then digested with XbaI and BglII, and
512 cloned into the corresponding sites in EYFP2-SV40NLS-NES. All plasmids were verified by Sanger
513 sequencing. See Supplementary Methods for additional details.

514

515 **Data analysis and statistics**

516 Statistical information, including mean and statistical significance values is indicated in the figures
517 or figure legends. At least three biological replicates were used per experiment. For analysis of
518 immunocytochemistry images, ROIs for nucleus and cytoplasm were either generated using CVAT
519 (68) or manually drawn in ImageJ. Nuclear/cytoplasmic ratio was calculated and statistical
520 significance was determined with GraphPadP Prism 9 using the tests indicated in each figure. Data
521 were considered statistically significant at *P < 0.05, **P < 0.01, ***P < 0.001 and ****P < 0.0001.
522 Data from Liu et al. was analyzed with assistance from the TDP43 loss of function database (69);
523 DESeq2 *P*-values were calculated using Wald tests and corrected for multiple testing using the
524 Benjamini–Hochberg method. DEU events with *P*adj <0.05 were considered significantly changed.

525

526 **Study approval**

527 Skin samples for iPSC creation were collected and de- identified in collaboration with the Michigan
528 Institute for Clinical and Health Research (MICHR, UL1TR000433) through an institutional review
529 board (IRB)-approved protocol (HUM00028826).

530

531 **Data availability**

All correspondence regarding the materials and data presented in this paper should be addressed to sbarmada@med.umich.edu.

Author Contributions

MB and SB designed the study. EP and MB designed experiments with SB. MB and EP collected data for most experimental studies, analyzed the data, assembled the figures, and wrote the manuscript. MB and EP performed immunocytochemistry. JM assisted with data collection and analysis. MB performed survival assays in cultured rat neurons and iNeurons, wrote custom FIJI scripts for quantitation of immunocytochemistry and dual IHC. EP made YFP reporter constructs, supervised dual IHC (with the IHC core),and selected motor neurons for quantitation. LGG and MM contributed to mbOrg concept, development, and data analysis. MK and SC cultured mbOrgs and performed RNASeq and qPCR. EU contributed to original concept and development of mbOrgs, and provided RNA-seq data from mbOrgs. XL isolated and cultured rat cortical neurons. EMHT derived iPSC lines and developed protocols for their differentiation. JW developed original code for neuron segmentation and image processing. SB provided resources, funding, and conceptual input for experiments and supervised the research. All authors were involved throughout the research process, agreed amongst themselves regarding roles and responsibilities, and contributed to the review, editing, and approval of the manuscript.

Acknowledgements

This work was supported by: National Institutes of Health AWD012778 (EP), National Institutes of Health (R01NS097542, R01NS113943 and 1R56NS128110-01 to SJB; R44NS124457 to MM;

554 P30AG072931 to the University of Michigan Brain Bank and Alzheimer's Disease Research
555 CenterNational Institute on Drug Abuse R44NS124457 (MDM and EMU), the family of Angela
556 Dobson and Lyndon Welch, the A. Alfred Taubman Medical Research Institute, the Danto Family,
557 Ann Arbor Active Against ALS, and the Robert Packard Center for ALS Research.

558 We thank all members of the Barmada laboratory for their advice and suggestions. We thank Dr.
559 Dafydd Thomas of the Rogel Cancer Center Tissue and Molecular Pathology Shared Resource
560 Laboratory at the University of Michigan (NIH P30 CA04659229). We thank the Michigan Institute for
561 Clinical and Health Research (MICHR, UL1TR000433), who collaborated to collect and de-identify
562 skin samples for iPSC creation. Finally, we thank the patients that donated tissue samples to make
563 this work possible.

564 Schematics were created in BioRender. Barmada, S. (2024) BioRender.com/z94b294

Figure 1

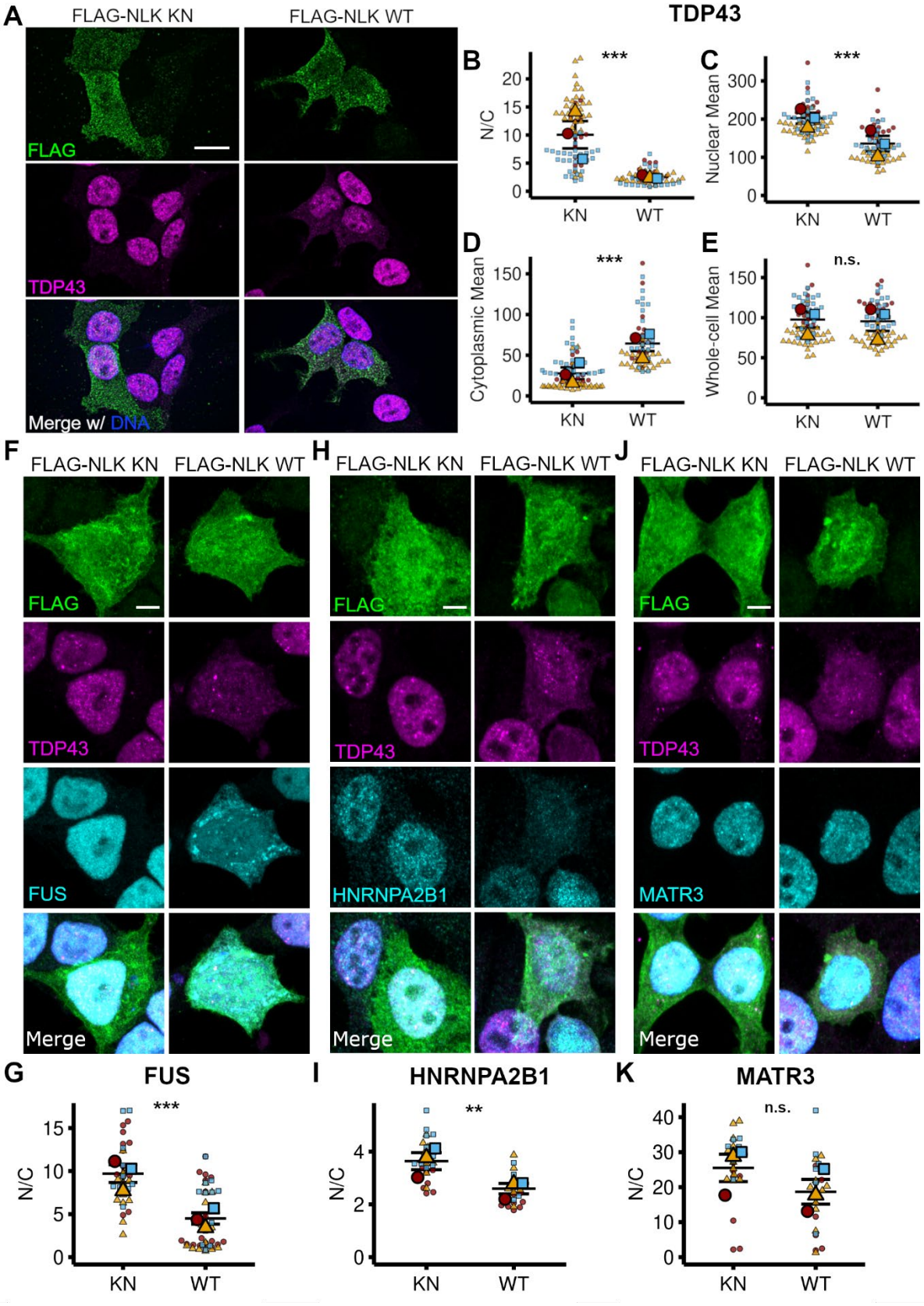
A
FLAG-NLK KN
FLAG-NLK WT
FLAG
TDP43
Merge w/ DNA
TDP43
B
N/C
***
KN
WT
C
Nuclear Mean
***
D
Cytoplasmic Mean
***
E
Whole-cell Mean
n.s.
F
FLAG-NLK KN
FLAG-NLK WT
FLAG
TDP43
FUS
Merge
H
HNRNPA2B1
J
MATR3
G
FUS
I
HNRNPA2B1
**
K
MATR3

565

566

567 **Figure 1. Overexpression of NLK leads to cytoplasmic accumulation of TDP43 and ALS-FTD**
568 **relevant RNA-binding proteins.** (**A**) HEK cells were transfected with plasmids encoding either
569 FLAG-NLK KN (KN; kinase-negative) or FLAG-NLK WT (WT; wild-type) followed by
570 immunofluorescence using antibodies against FLAG and TDP4343 while DNA was stained with
571 Hoechst. Scale bar = 10μm. (**B**) Superplot of Nuclear-Cytoplasmic ratio (N/C) of TDP43 from
572 images in (A). Line = mean, error bar = standard error. *p<0.05, ** p<0.01, ***p<0.001. (unpaired T-
573 test with Welch's correction). (**C**) Superplot of TDP43 nuclear intensity in cells that overexpress KN
574 or WT NLK. Line = mean, error bar = standard error. (**D**) Superplot of TDP43 cytoplasmic intensity in
575 cells that overexpress KN or WT NLK. Line = mean, error bar = standard error. (**E**) Superplot
576 quantification of TDP43 whole-cell intensity in cells that overexpress KN or WT NLK. Line = mean,
577 error bar = standard error. (**F**) HEK cells were transfected with the indicated FLAG-NLK plasmids as
578 in (A) followed by immunofluorescence using antibodies against FLAG, TDP43, and FUS while DNA
579 was stained with Hoechst. Scale bar = 10μm (**G**) Superplot of FUS localization in cells that
580 overexpress KN or WT NLK. Line = mean, error bar = standard error. (**H**) HEK cells were transfected
581 with the indicated FLAG-NLK plasmids as in (A) followed by immunofluorescence using antibodies
582 against FLAG, TDP43, and HNRNPA2B1 while DNA was stained with Hoechst. Scale bar = 10μm. (**I**)
583 Superplot of HNRNPA2B1 localization in cells that overexpress KN or WT NLK. Line = mean, error
584 bar = standard error. (**J**) HEK cells were transfected with the indicated FLAG-NLK plasmids as in (A)
585 followed by immunofluorescence using antibodies against FLAG, TDP43, and MATR3 while DNA
586 was stained with Hoechst. Scale bar = 10μm. (**K**) HEK cells were transfected with the indicated
587 FLAG-NLK plasmids as in (A) followed by immunofluorescence using antibodies against FLAG and
588 MART3 while DNA was stained with Hoechst. Scale bar = 10μm. (**L**) Superplot of HNRNPA2B1
589 localization in cells that overexpress KN or WT NLK. Line = mean, error bar = standard error.

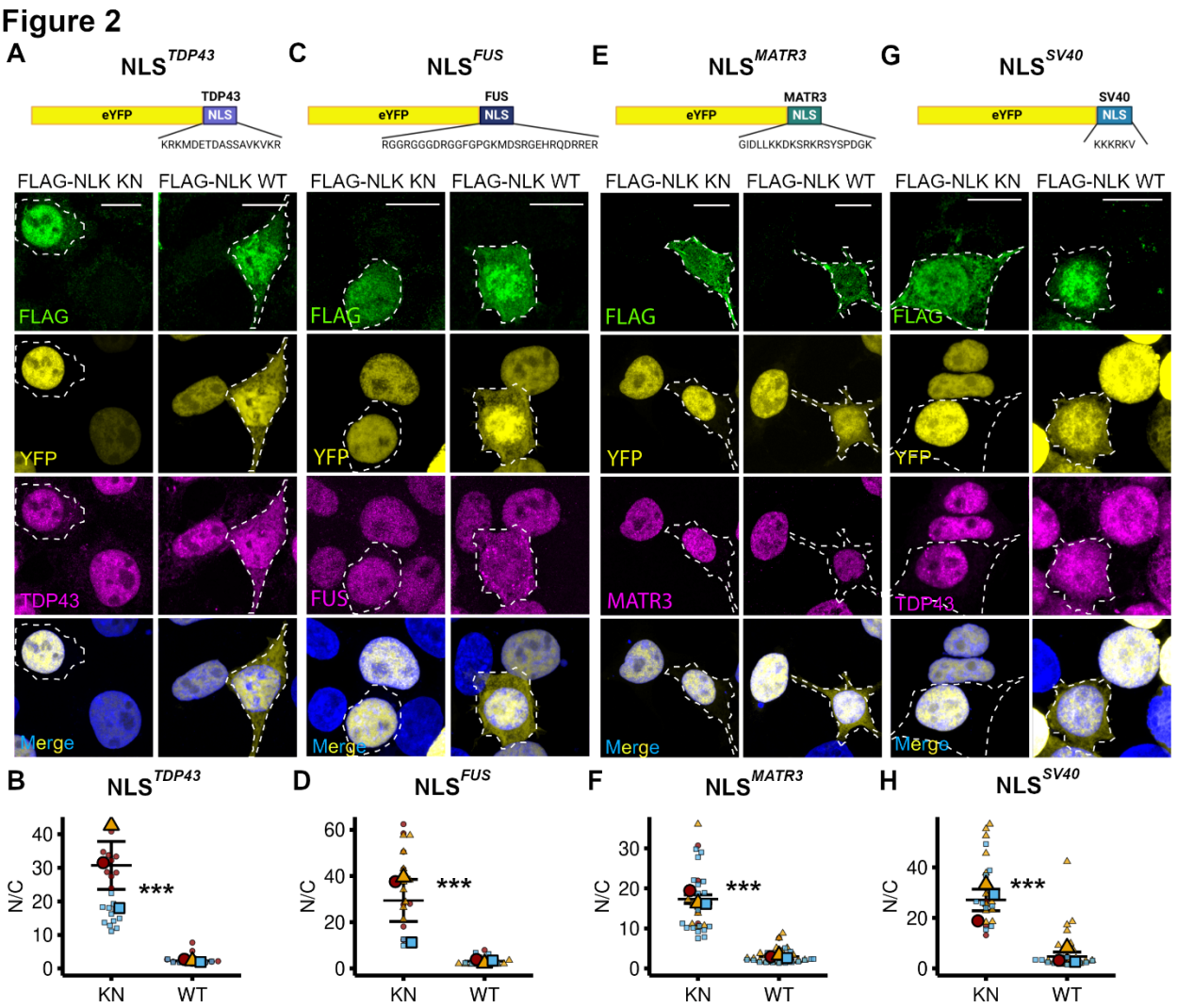

590

591

592 **Figure 2. NLK overexpression disrupts NLS dependent nuclear import.** (**A-D**) HEK cells were co-

593 transfected with plasmids encoding either FLAG-NLK KN or FLAG-NLK WT and either of the

594 following NLS-reporter eYFP-NLS^{TDP43} (A), eYFP-NLS^{FUS} (B), eYFP-NLS^{MATR3} (C), or eYFP-NLS^{SV40}.

595 Schematics created in BioRender. (D). Immunofluorescence was performed using antibodies

596 against FLAG and either TDP43, FUS, or Matrin-3 while DNA was stained with Hoechst. Scale bar 10

597 uM. (**E-H**) Superplot of NLS-reporter Nuclear-Cytoplasmic ratio (N/C) from images in A-D. Line =

598 mean, error bar= standard error. *** indicates p-value < 0.001 (unpaired t-test with Welch's

599 correction).

600

Figure 3

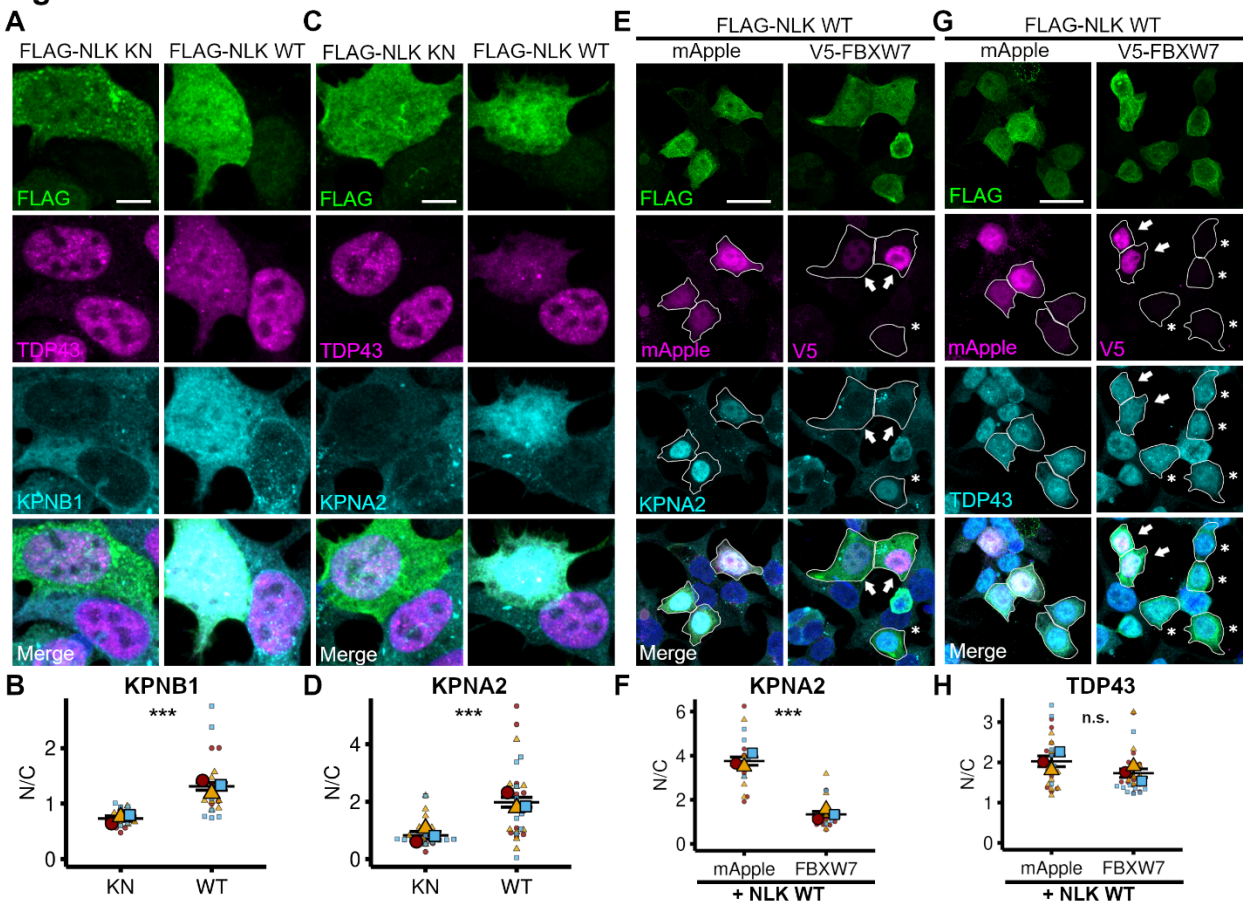

Figure 3. NLK-dependent mislocalization of TDP43 does not depend on nuclear accumulation of KPNA2 and KPNB1. (**A**) HEK cells were transfected with plasmids encoding either FLAG-NLK KN (KN; kinase-negative) or FLAG-NLK WT (WT; wild-type) followed by immunofluorescence using antibodies against FLAG, TDP43, and KPNA2 or KPNB1 while DNA was stained with Hoechst. Scale bar = 5μm. (**B**) Quantification of KPNA2 and KPNB1 localization in cells that overexpress NLK KN or WT. Line = mean, error bar = standard error. Statistical significance indicated as such in all sub-panels: n.s. = not significant, *p<0.05, ** p<0.01, ***p<0.001(unpaired t-test with Welch's correction).(**C**) HEK cells were co- transfected with plasmids encoding FLAG-NLK WT and either mApple (negative-control) or V5-FBXW7 followed by immunofluorescence using antibodies against

612 KPNA2, FLAG, and V5 while DNA was stained with Hoechst. Scale bar = 20μm. (**D**) Quantification of
613 KPNA2 localization in cells that overexpress FLAG-NLK WT and either mApple or V5-FBXW7. Line=
614 mean, error bar= standard error. *p<0.05, ** p<0.01, ***p<0.001 (unpaired t-test with Welch's
615 correction). (**E**) HEK cells were co-transfected with plasmids encoding FLAG-NLK WT and either
616 mApple or V5-FBXW7 followed by immunofluorescence using antibodies against TDP43, FLAG, and
617 V5 while DNA was stained with Hoechst. Scale bar = 20μm. (**F**) Quantification of TDP43 localization
618 in cells that overexpress FLAG-NLK WT and either mApple or V5-FBXW7. Line = mean, error bar=
619 standard error. *p<0.05, ** p<0.01, ***p<0.001 (unpaired t-test with Welch's correction). (G) HEK
620 cells were co-transfected as in E) followed by immunofluorescence using antibodies against
621 KPNA2, FLAG, and V5 while DNA was stained with Hoescht. Scale bar = 20 μm.(H) HEK cells were
622 co- transfected as in E) followed by immunofluorescence using antibodies against KPNA2, FLAG,
623 and V5 while DNA was stained with Hoechst. Scale bar = 20μm. (I) Quantification of KPNB1
624 localization in cells that overexpress NLK WT and either mApple orr V5-FBXW7. Line = mean, error
625 bar = standard error.

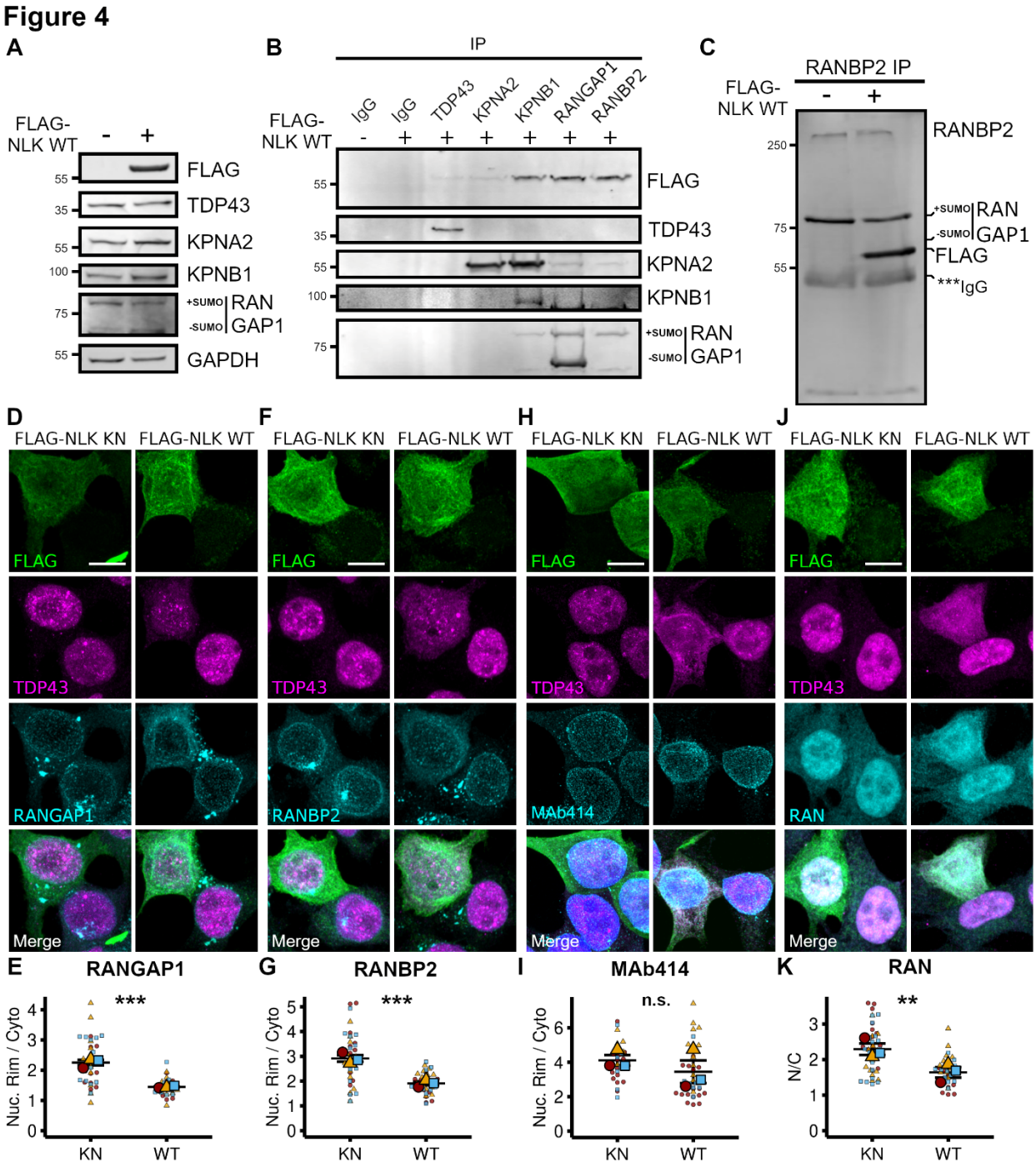

Figure 4. NLK overexpression mislocalizes RanBP2-RanGAP1 and disrupts the Ran gradient. (**A**) Representative western blots from HEK cells transfected with either vector (-) or FLAG-NLK WT (WT, +; wild-type). #'s to the left represent molecular weight in kDa. (**B**) Western blots after

631 immunoprecipitation (IP) using 1μg of the indicated antibodies in 1mg of lysates from (A). (**C**)
632 Western blots after RanBP2 co-IP from lysates in (A) were run on a 4-20% tris-glycine gel to
633 facilitate visualization of RanBP2 and validate NLK complex formation with RanBP2-RanGAP1-
634 SUMO. (**D**) HEK cells were transfected with plasmids encoding either FLAG-NLK KN (KN; kinase-
635 negative) or FLAG-NLK WT (WT; wild-type) followed by immunofluorescence using antibodies
636 against FLAG, TDP43, and either Ran, RanGAP1, RanBP2, or MAb414 (FG-nucleoporins) while DNA
637 was stained with Hoechst. Scale bar = 10μm. (**E**) Superplot of nuclear-cytoplasmic ratio (N/C) of
638 Ran. Line = mean, error bar= standard error. Statistical significance indicated as such in all sub-
639 panels: n.s. = not significant, *p<0.05, ** p<0.01, ***p<0.001. *p<0.05, ** p<0.01, ***p<0.001
640 (unpaired t-test with Welch's correction). (**F**) HEK cells were transfected as in (D) followed by
641 immunofluorescence using antibodies against FLAG, TDP43, and RANBP2 while DNA was stained
642 with Hoechst. Scale bar = 10μm. (**G**) Superplot of nuclear-rim-cytoplasm ratio (Nuc. Rim/Cyto) of
643 RANBP2. (**H**) HEK cells were transfected as in (D) followed by immunofluorescence using
644 antibodies against FLAG, TDP43, and MAB414 (FG-nucleoporins) while DNA was stained with
645 Hoechst. Scale bar = 10μm. (**I**) Superplot of nuclear-rim-cytoplasm ratio (Nuc. Rim/Cyto) of
646 MAB414. (**J**) HEK cells were transfected as in (D) followed by immunofluorescence using antibodies
647 against FLAG, TDP43, and RAN while DNA was stained with Hoechst. Scale bar = 10μm. (**K**)
648 Superplot quantification of nuclear-cytoplasm ratio (N/C) of RAN.

Figure 5

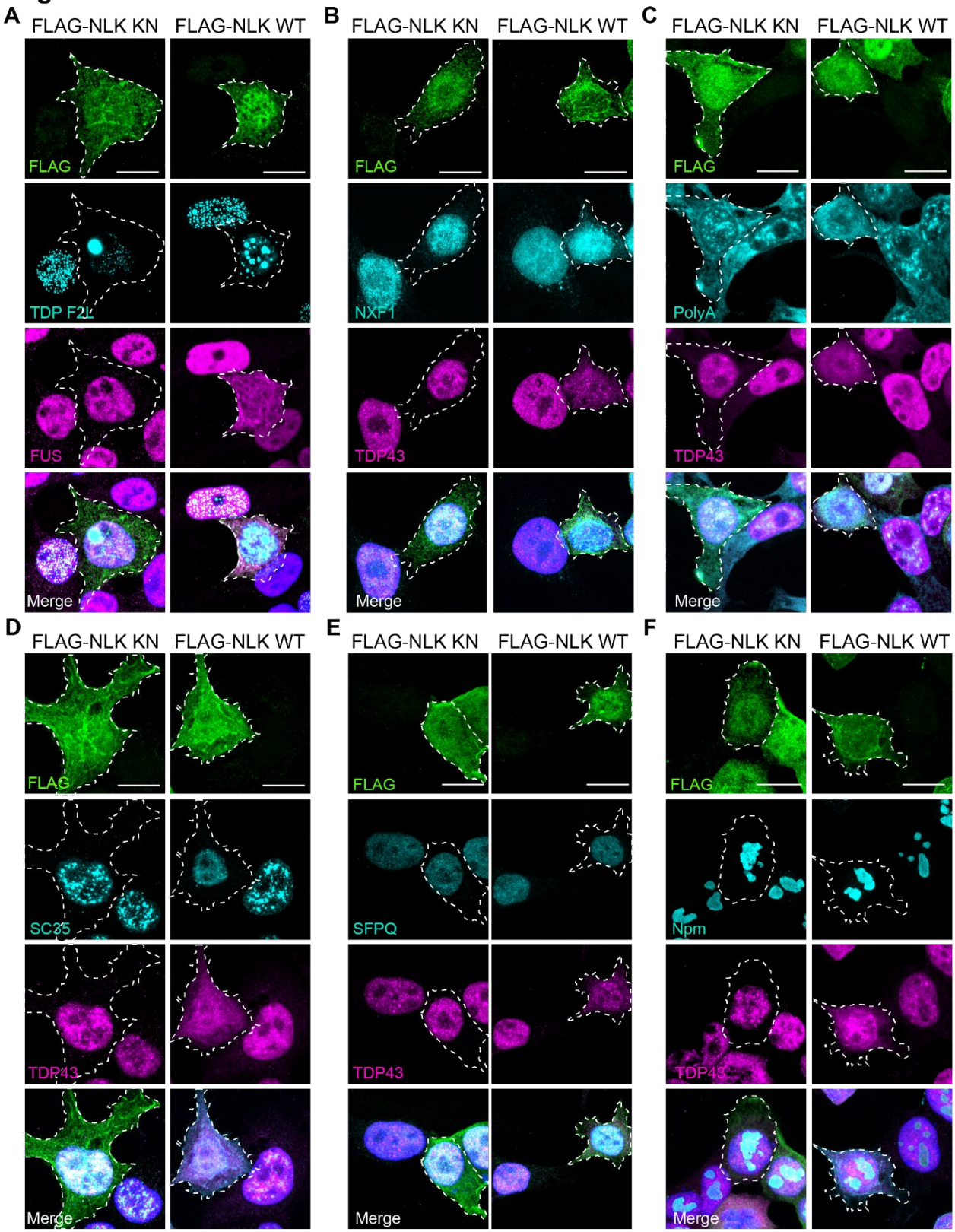

649

650

651 **Figure 5. NLK overexpression drives dissolution of nuclear speckles.** (**A**) HEK cells were co-
652 transfected with plasmids encoding either FLAG-NLK KN or FLAG-NLK WT and a GFP-tagged RNA-
653 binding mutant TDP43 (TDP43 F147/9L; F2L) followed by immunofluorescence using antibodies
654 against FLAG and FUS and direct visualization of tagged protein while DNA was stained with
655 Hoechst. Scale bar 10 μm. (**B**) HEK cells were transfected with plasmids encoding either FLAG-NLK
656 KN or FLAG-NLK WT followed by immunofluorescence using antibodies against FLAG, TDP43, and
657 NXF1. Scale bar 10 μm. (**C**) HEK cells were transfected with plasmids encoding either FLAG-NLK
658 KN or FLAG-NLK WT followed by polyA FISH and immunofluorescence for TDP43. Scale bar 10 μm.
659 (**D-F**) HEK cells were transfected with plasmids encoding either FLAG-NLK KN or FLAG-NLK WT
660 followed by immunofluorescence for TDP43 and markers of speckles (SC-35) (D), paraspeckles
661 (SFPQ) (E), or nucleolus (nucleophosmin, Npm) (F). Scale bar 10 μm.

Figure 6

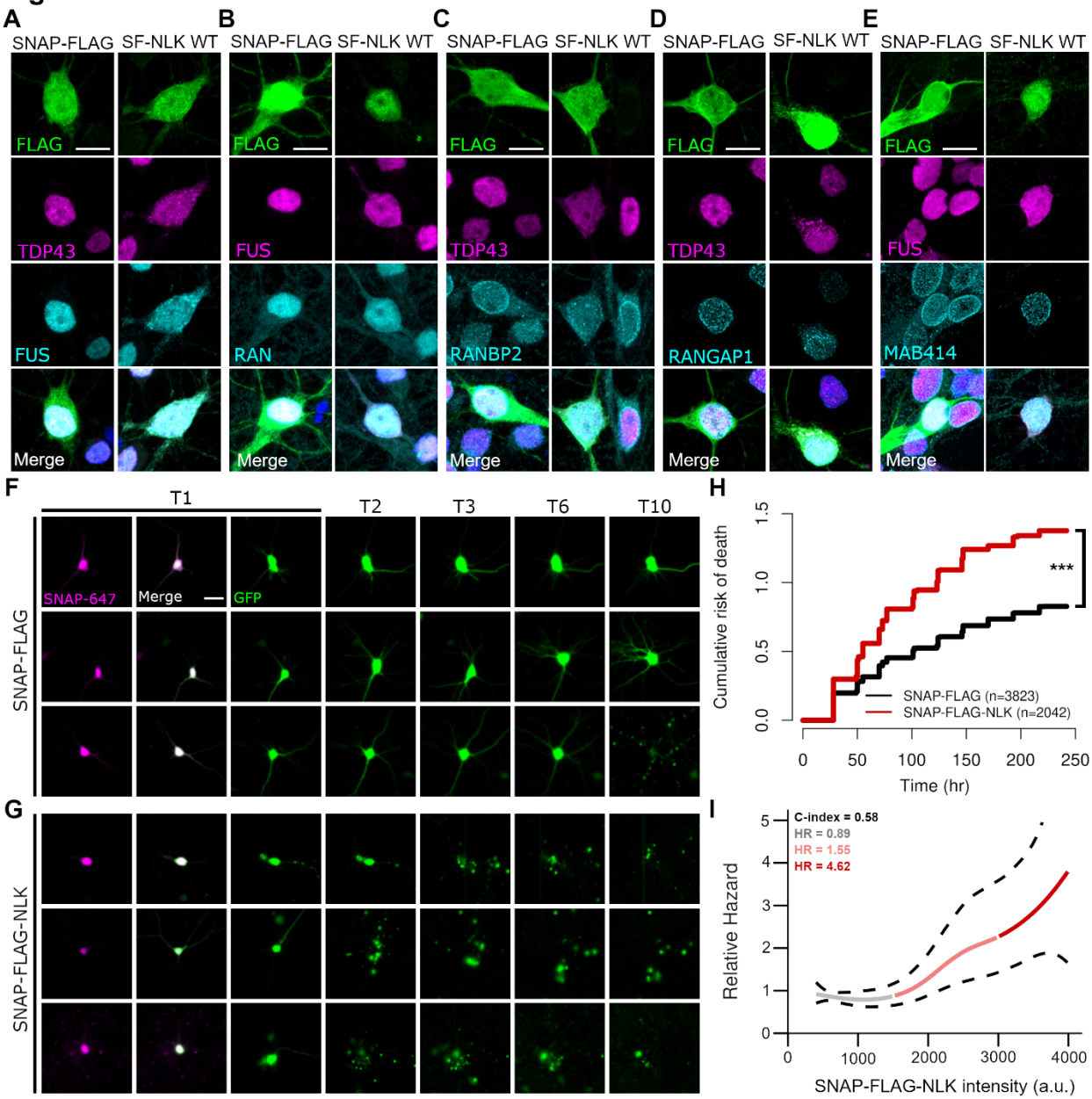

Figure 6. NLK overexpression disrupts nuclear import and is toxic in primary rat neurons. (**A**) Rodent primary cortical neurons were transfected with either SNAP-FLAG (SF; negative-control) or SNAP-FLAG-NLK (SF-NLK) followed by immunofluorescence using antibodies against FLAG and either TDP43, FUS, Ran, RanBP2, RanGAP1, and Mab414 while DNA was stained with Hoechst.Scale bar = 10 µm. (**B**) Rodent primary cortical neurons were co-transfected with plasmids

669 encoding either SF or SF-NLK and EGFP (survival marker), treated with SNAP-647 dye at T1 to
670 visualize SNAP-positive neurons, and tracked by longitudinal microscopy to determine neuron fate
671 (see methods). Scale bar = 20μm. (**C**) Cumulative Hazard plot showing the relative risk of death in
672 neurons that express either SF or SF-NLK. Hazard ratio = 1.616. ***p=1.494e-59. (**D**) Cox
673 proportional hazards model predicting relative hazard associated with different intensities of
674 SNAP-FLAG-NLK. Solid lines indicate the estimated hazard, with color gradients corresponding to
675 intensity levels: grey (low intensity), light red (medium intensity), and red (high intensity). Dashed
676 lines represent 95% confidence intervals for hazard estimates.

Figure 7

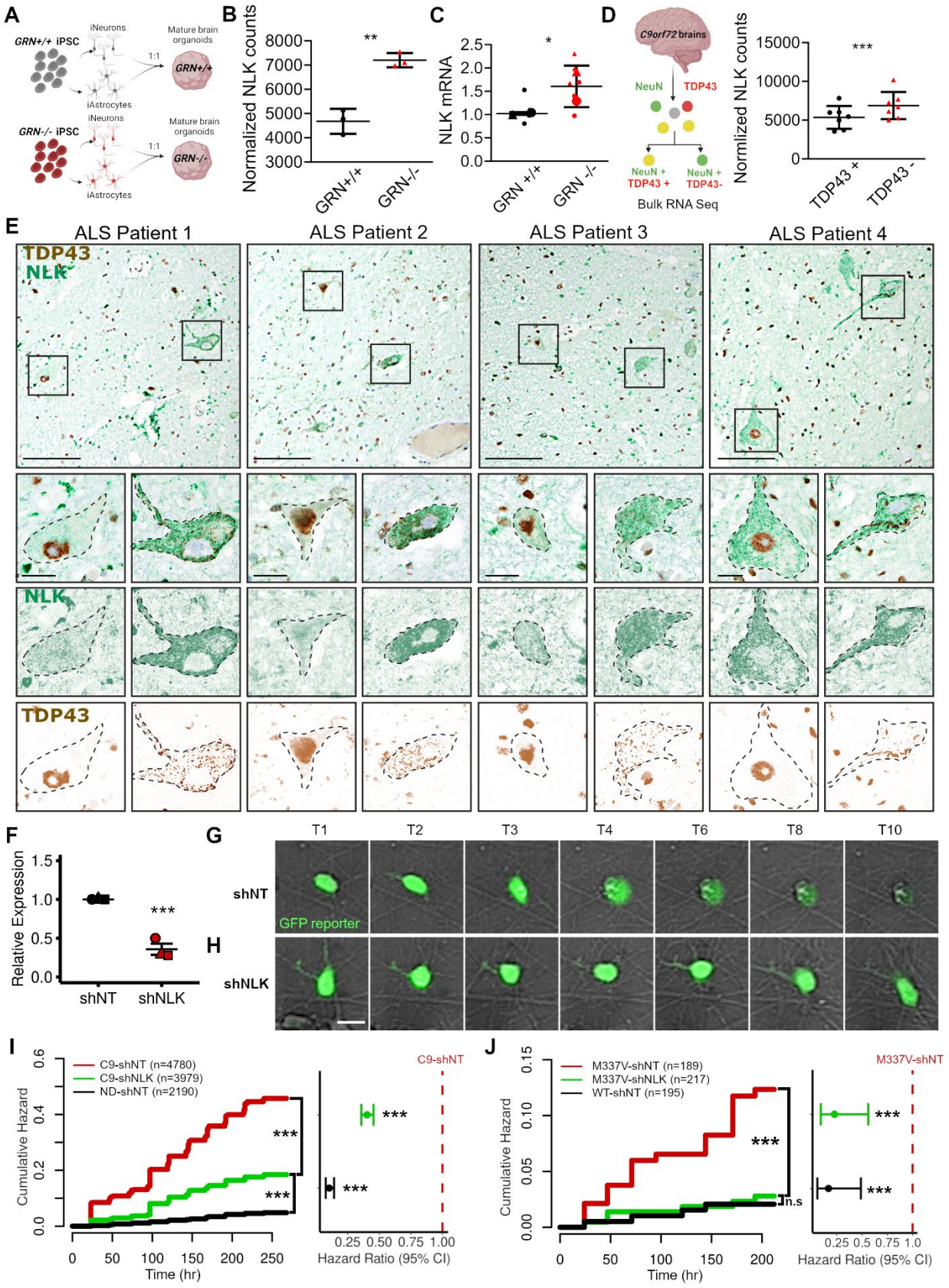
A
GRN+/+ iPSC
iNeurons
iAstrocytes
Mature brain organoids
1:1
GRN+/+
GRN-/- iPSC
GRN-/-
B
Normalized NLK counts
GRN+/+
GRN-/-
C
NLK mRNA
GRN +/+
GRN -/-
D
C9orf72 brains
NeuN
TDP43
NeuN + TDP43 +
NeuN + TDP43-
Bulk RNA Seq
Normlized NLK counts
TDP43 +
TDP43 -
E
ALS Patient 1
ALS Patient 2
ALS Patient 3
ALS Patient 4
TDP43
NLK
F
Relative Expression
shNT
shNLK
G
H
T1
T2
T3
T4
T6
T8
T10
GFP reporter
I
C9-shNT (n=4780)
C9-shNLK (n=3979)
ND-shNT (n=2190)
Cumulative Hazard
Time (hr)
Hazard Ratio (95% CI)
J
M337V-shNT (n=189)
M337V-shNLK (n=217)
WT-shNT (n=195)
n.s

677

678

679 **Figure 7. TDP43 pathology is associated with NLK overexpression in human model systems**
680 **and patient samples.** (**A**) Schematic of generation of mbOrgs. (**B**) Normalized NLK counts from
681 RNASeq performed on WT or GRN$^{-/-}$ mbOrgs. Line = mean, error bar = standard deviation. ** p< 0.01
682 (unpaired t-test with Welch's correction). (**C**) QPCR was performed on WT or GRN$^{-/-}$ mbOrgs (2
683 biological replicates, 3 technical replicates). Superplot of NLK levels normalized to GAPDH. Line =
684 mean, error bar = standard deviation. * p<0.05 (unpaired t-test with Welch's correction). (**D**) NLK
685 normalized counts from RNAseq performed on TDP positive and negative nuclei. Line = mean, error
686 bar = standard deviation. **** p<0.001 (Wald tests, corrected for multiple testing using the
687 Benjamini–Hochberg method). (**E**) Dual immunohistochemistry for NLK and TDP43, performed on
688 spinal cord tissue from four patients with sporadic ALS. Images deconvolved using FIJI. Upper
689 panels: scale bar 100 µm. Lower panels: scale bar 20 µm. (**F**) Quantitative real-time PCR of NLK
690 mRNA levels in iPSC derived neurons after transduction with lentivirus virus encoding either non-
691 targeting shRNA (shNT) or NLK shRNA (shNLK). Line = mean, error bar = standard error. *** p<
692 0.001 (unpaired t-test with Welch's correction). (**G**) Isogenic (WT) and mutant TDP43 (M337V) iPSC-
693 derived neurons were transduced with virus encoding either non targeting (NT) shRNA or NLK
694 shRNA followed by longitudinal microscopy to track neuron fate (see methods). Scale bar = 20 µm.
695 (**H**) Cumulative Hazard plot showing the relative risk of death in ND and C9 neurons that express
696 either shNT shRNA or shNLK (HR = 0.4, p<0.001). (**I**) Cumulative Hazard plot showing the relative
697 risk of death in WT and M337V neurons that express either Scramble shRNA or NLKshRNA. (HR =
698 0.23, p=0.0013).

699 **References**

700 1. Brown RH, and Al-Chalabi A. Amyotrophic Lateral Sclerosis. *N Engl J Med*.
701 2017;377(16):1602.
702 2. Tan RH, Ke YD, Ittner LM, and Halliday GM. ALS/FTLD: experimental models and reality.
703 *Acta Neuropathol*. 2017;133(2):177-96.
704 3. Neumann M, Sampathu DM, Kwong LK, Truax AC, Micsenyi MC, Chou TT, et al.
705 Ubiquitinated TDP-43 in frontotemporal lobar degeneration and amyotrophic lateral
706 sclerosis. *Science*. 2006;314(5796):130-3.
707 4. Alami NH, Smith RB, Carrasco MA, Williams LA, Winborn CS, Han SSW, et al. Axonal
708 transport of TDP-43 mRNA granules is impaired by ALS-causing mutations. *Neuron*.
709 2014;81(3):536-43.
710 5. Ling JP, Pletnikova O, Troncoso JC, and Wong PC. TDP-43 repression of nonconserved
711 cryptic exons is compromised in ALS-FTD. *Science*. 2015;349(6248):650-5.
712 6. Polymenidou M, Lagier-Tourenne C, Hutt KR, Huelga SC, Moran J, Liang TY, et al. Long pre-
713 mRNA depletion and RNA missplicing contribute to neuronal vulnerability from loss of TDP-
714 43. *Nat Neurosci*. 2011;14(4):459-68.
715 7. Tank EM, Figueroa-Romero C, Hinder LM, Bedi K, Archbold HC, Li X, et al. Abnormal RNA
716 stability in amyotrophic lateral sclerosis. *Nat Commun*. 2018;9(1):2845.
717 8. Takeuchi R, Toyoshima Y, Tada M, Shiga A, Tanaka H, Shimohata M, et al. Transportin 1
718 accumulates in FUS inclusions in adult-onset ALS without FUS mutation. *Neuropathol Appl*
719 *Neurobiol*. 2013;39(5):580-4.
720 9. Freibaum BD, Lu Y, Lopez-Gonzalez R, Kim NC, Almeida S, Lee KH, et al. GGGGCC repeat
721 expansion in C9orf72 compromises nucleocytoplasmic transport. *Nature*.
722 2015;525(7567):129-33.

723 10. Jovičić A, Mertens J, Boeynaems S, Bogaert E, Chai N, Yamada SB, et al. Modifiers of
724 C9orf72 dipeptide repeat toxicity connect nucleocytoplasmic transport defects to FTD/ALS.
725 *Nat Neurosci*. 2015;18(9):1226-9.
726 11. Zhang K, Donnelly CJ, Haeusler AR, Grima JC, Machamer JB, Steinwald P, et al. The C9orf72
727 repeat expansion disrupts nucleocytoplasmic transport. *Nature*. 2015;525(7567):56-61.
728 12. Thorpe CJ, and Moon RT. nemo-like kinase is an essential co-activator of Wnt signaling
729 during early zebrafish development. *Development*. 2004;131(12):2899-909.
730 13. Yasuda J, Tsuchiya A, Yamada T, Sakamoto M, Sekiya T, and Hirohashi S. Nemo-like kinase
731 induces apoptosis in DLD-1 human colon cancer cells. *Biochem Biophys Res Commun*.
732 2003;308(2):227-33.
733 14. Emami KH, Brown LG, Pitts TE, Sun X, Vessella RL, and Corey E. Nemo-like kinase induces
734 apoptosis and inhibits androgen receptor signaling in prostate cancer cells. *Prostate*.
735 2009;69(14):1481-92.
736 15. Tejwani L, Jung Y, Kokubu H, Sowmithra S, Ni L, Lee C, et al. Reduction of nemo-like kinase
737 increases lysosome biogenesis and ameliorates TDP-43-related neurodegeneration. *J Clin*
738 *Invest*. 2023;133(16).
739 16. Ju H, Kokubu H, Todd TW, Kahle JJ, Kim S, Richman R, et al. Polyglutamine disease toxicity
740 is regulated by Nemo-like kinase in spinocerebellar ataxia type 1. *J Neurosci*.
741 2013;33(22):9328-36.
742 17. Todd TW, Kokubu H, Miranda HC, Cortes CJ, La Spada AR, and Lim J. Nemo-like kinase is a
743 novel regulator of spinal and bulbar muscular atrophy. *Elife*. 2015;4:e08493.
744 18. Jiang M, Zhang X, Liu H, LeBron J, Alexandris A, Peng Q, et al. Nemo-like kinase reduces
745 mutant huntingtin levels and mitigates Huntington's disease. *Hum Mol Genet*.
746 2020;29(8):1340-52.

747 19. Brott BK, Pinsky BA, and Erikson RL. Nlk is a murine protein kinase related to Erk/MAP
748 kinases and localized in the nucleus. *Proc Natl Acad Sci U S A*. 1998;95(3):963-8.
749 20. Lee BJ, Cansizoglu AE, Süel KE, Louis TH, Zhang Z, and Chook YM. Rules for nuclear
750 localization sequence recognition by karyopherin beta 2. *Cell*. 2006;126(3):543-58.
751 21. Winton MJ, Igaz LM, Wong MM, Kwong LK, Trojanowski JQ, and Lee VM. Disturbance of
752 nuclear and cytoplasmic TAR DNA-binding protein (TDP-43) induces disease-like
753 redistribution, sequestration, and aggregate formation. *J Biol Chem*. 2008;283(19):13302-9.
754 22. Hisada-Ishii S, Ebihara M, Kobayashi N, and Kitagawa Y. Bipartite nuclear localization signal
755 of matrin 3 is essential for vertebrate cells. *Biochem Biophys Res Commun*.
756 2007;354(1):72-6.
757 23. Ederle H, Funk C, Abou-Ajram C, Hutten S, Funk EBE, Kehlenbach RH, et al. Nuclear egress
758 of TDP-43 and FUS occurs independently of Exportin-1/CRM1. *Sci Rep*. 2018;8(1):7084.
759 24. Pinarbasi ES, Cağatay T, Fung HYJ, Li YC, Chook YM, and Thomas PJ. Active nuclear import
760 and passive nuclear export are the primary determinants of TDP-43 localization. *Sci Rep*.
761 2018;8(1):7083.
762 25. Archbold HC, Jackson KL, Arora A, Weskamp K, Tank EM, Li X, et al. TDP43 nuclear export
763 and neurodegeneration in models of amyotrophic lateral sclerosis and frontotemporal
764 dementia. *Sci Rep*. 2018;8(1):4606.
765 26. Dormann D, Rodde R, Edbauer D, Bentmann E, Fischer I, Hruscha A, et al. ALS-associated
766 fused in sarcoma (FUS) mutations disrupt Transportin-mediated nuclear import. *EMBO J*.
767 2010;29(16):2841-57.
768 27. Görlich D, Vogel F, Mills AD, Hartmann E, and Laskey RA. Distinct functions for the two
769 importin subunits in nuclear protein import. *Nature*. 1995;377(6546):246-8.

770 28. Xing Z, Zhen Y, Chen J, Du M, Li D, Liu R, et al. KPNA2 Silencing, Regulated by E3 Ubiquitin
771 Ligase FBXW7, Alleviates Endothelial Dysfunction and Inflammation Through Inhibiting the
772 Nuclear Translocation of p65 and IRF3: A Possible Therapeutic Approach for
773 Atherosclerosis. *Inflammation*. 2023;46(6):2071-88.
774 29. Stewart M. Molecular mechanism of the nuclear protein import cycle. *Nat Rev Mol Cell Biol*.
775 2007;8(3):195-208.
776 30. Varjosalo M, Keskitalo S, Van Drogen A, Nurkkala H, Vichalkovski A, Aebersold R, et al. The
777 protein interaction landscape of the human CMGC kinase group. *Cell Rep*. 2013;3(4):1306-
778 20.
779 31. Mahajan R, Delphin C, Guan T, Gerace L, and Melchior F. A small ubiquitin-related
780 polypeptide involved in targeting RanGAP1 to nuclear pore complex protein RanBP2. *Cell*.
781 1997;88(1):97-107.
782 32. Saitoh H, Pu R, Cavenagh M, and Dasso M. RanBP2 associates with Ubc9p and a modified
783 form of RanGAP1. *Proc Natl Acad Sci U S A*. 1997;94(8):3736-41.
784 33. Matunis MJ, Coutavas E, and Blobel G. A novel ubiquitin-like modification modulates the
785 partitioning of the Ran-GTPase-activating protein RanGAP1 between the cytosol and the
786 nuclear pore complex. *J Cell Biol*. 1996;135(6 Pt 1):1457-70.
787 34. Duan L, Zaepfel BL, Aksenova V, Dasso M, Rothstein JD, Kalab P, et al. Nuclear RNA binding
788 regulates TDP-43 nuclear localization and passive nuclear export. *Cell Rep*.
789 2022;40(3):111106.
790 35. Buratti E, and Baralle FE. Characterization and functional implications of the RNA binding
791 properties of nuclear factor TDP-43, a novel splicing regulator of CFTR exon 9. *J Biol Chem*.
792 2001;276(39):36337-43.

793 36. Flores BN, Li X, Malik AM, Martinez J, Beg AA, and Barmada SJ. An Intramolecular Salt Bridge
794 Linking TDP43 RNA Binding, Protein Stability, and TDP43-Dependent Neurodegeneration.
795 *Cell Rep*. 2019;27(4):1133-50.e8.
796 37. Pérez-Berlanga M, Wiersma VI, Zbinden A, De Vos L, Wagner U, Foglieni C, et al. Loss of
797 TDP-43 oligomerization or RNA binding elicits distinct aggregation patterns. *EMBO J*.
798 2023;42(17):e111719.
799 38. Ilik İ, Malszycki M, Lübke AK, Schade C, Meierhofer D, and Aktaş T. SON and SRRM2 are
800 essential for nuclear speckle formation. *Elife*. 2020;9.
801 39. Imamura K, Imamachi N, Akizuki G, Kumakura M, Kawaguchi A, Nagata K, et al. Long
802 noncoding RNA NEAT1-dependent SFPQ relocation from promoter region to paraspeckle
803 mediates IL8 expression upon immune stimuli. *Mol Cell*. 2014;53(3):393-406.
804 40. Mitrea DM, Cika JA, Guy CS, Ban D, Banerjee PR, Stanley CB, et al. Nucleophosmin
805 integrates within the nucleolus via multi-modal interactions with proteins displaying R-rich
806 linear motifs and rRNA. *Elife*. 2016;5.
807 41. Arrasate M, Mitra S, Schweitzer ES, Segal MR, and Finkbeiner S. Inclusion body formation
808 reduces levels of mutant huntingtin and the risk of neuronal death. *Nature*.
809 2004;431(7010):805-10.
810 42. Barmada SJ, Serio A, Arjun A, Bilican B, Daub A, Ando DM, et al. Autophagy induction
811 enhances TDP43 turnover and survival in neuronal ALS models. *Nat Chem Biol*.
812 2014;10(8):677-85.
813 43. Barmada SJ, Ju S, Arjun A, Batarse A, Archbold HC, Peisach D, et al. Amelioration of toxicity
814 in neuronal models of amyotrophic lateral sclerosis by hUPF1. *Proc Natl Acad Sci U S A*.
815 2015;112(25):7821-6.

816 44. Miller J, Arrasate M, Shaby BA, Mitra S, Masliah E, and Finkbeiner S. Quantitative
817 relationships between huntingtin levels, polyglutamine length, inclusion body formation,
818 and neuronal death provide novel insight into huntington's disease molecular
819 pathogenesis. *J Neurosci*. 2010;30(31):10541-50.
820 45. Strong MJ, Abrahams S, Goldstein LH, Woolley S, Mclaughlin P, Snowden J, et al.
821 Amyotrophic lateral sclerosis - frontotemporal spectrum disorder (ALS-FTSD): Revised
822 diagnostic criteria. *Amyotroph Lateral Scler Frontotemporal Degener*. 2017;18(3-4):153-74.
823 46. de Majo M, Koontz M, Marsan E, Salinas N, Ramsey A, Kuo YM, et al. Granulin loss of
824 function in human mature brain organoids implicates astrocytes in TDP-43 pathology. *Stem*
825 *Cell Reports*. 2023;18(3):706-19.
826 47. DeJesus-Hernandez M, Mackenzie IR, Boeve BF, Boxer AL, Baker M, Rutherford NJ, et al.
827 Expanded GGGGCC hexanucleotide repeat in noncoding region of C9ORF72 causes
828 chromosome 9p-linked FTD and ALS. *Neuron*. 2011;72(2):245-56.
829 48. Morita M, Al-Chalabi A, Andersen PM, Hosler B, Sapp P, Englund E, et al. A locus on
830 chromosome 9p confers susceptibility to ALS and frontotemporal dementia. *Neurology*.
831 2006;66(6):839-44.
832 49. McMillan M, Gomez N, Hsieh C, Bekier M, Li X, Miguez R, et al. RNA methylation influences
833 TDP43 binding and disease pathogenesis in models of amyotrophic lateral sclerosis and
834 frontotemporal dementia. *Mol Cell*. 2023;83(2):219-36.e7.
835 50. Boeynaems S, Bogaert E, Michiels E, Gijselinck I, Sieben A, Jovičić A, et al. Drosophila
836 screen connects nuclear transport genes to DPR pathology in c9ALS/FTD. *Sci Rep*.
837 2016;6:20877.

838 51. Hutten S, Flotho A, Melchior F, and Kehlenbach RH. The Nup358-RanGAP complex is
839 required for efficient importin alpha/beta-dependent nuclear import. *Mol Biol Cell*.
840 2008;19(5):2300-10.
841 52. Hong AW, Meng Z, Yuan HX, Plouffe SW, Moon S, Kim W, et al. Osmotic stress-induced
842 phosphorylation by NLK at Ser128 activates YAP. *EMBO Rep*. 2017;18(1):72-86.
843 53. Yuan HX, Wang Z, Yu FX, Li F, Russell RC, Jewell JL, et al. NLK phosphorylates Raptor to
844 mediate stress-induced mTORC1 inhibition. *Genes Dev*. 2015;29(22):2362-76.
845 54. Cargnello M, and Roux PP. Activation and function of the MAPKs and their substrates, the
846 MAPK-activated protein kinases. *Microbiol Mol Biol Rev*. 2011;75(1):50-83.
847 55. Peters S, Zitzelsperger E, Kuespert S, Iberl S, Heydn R, Johannesen S, et al. The TGF-β
848 System As a Potential Pathogenic Player in Disease Modulation of Amyotrophic Lateral
849 Sclerosis. *Front Neurol*. 2017;8:669.
850 56. Zhang N, Westerhaus A, Wilson M, Wang E, Goff L, and Sockanathan S. Physiological
851 regulation of neuronal Wnt activity is essential for TDP-43 localization and function. *EMBO*
852 *J*. 2024.
853 57. Ke H, Masoumi KC, Ahlqvist K, Seckl MJ, Rydell-Törmänen K, and Massoumi R. Nemo-like
854 kinase regulates the expression of vascular endothelial growth factor (VEGF) in alveolar
855 epithelial cells. *Sci Rep*. 2016;6:23987.
856 58. Kortenjann M, Nehls M, Smith AJ, Carsetti R, Schüler J, Köhler G, et al. Abnormal bone
857 marrow stroma in mice deficient for nemo-like kinase, Nlk. *Eur J Immunol*.
858 2001;31(12):3580-7.
859 59. Liu R, Khalil H, Lin SJ, Sargent MA, York AJ, and Molkentin JD. Nemo-Like Kinase (NLK) Is a
860 Pathological Signaling Effector in the Mouse Heart. *PLoS One*. 2016;11(10):e0164897.

861 60. Weskamp K, Tank EM, Miguez R, McBride JP, Gómez NB, White M, et al. Shortened TDP43
862 isoforms upregulated by neuronal hyperactivity drive TDP43 pathology in ALS. *J Clin Invest*.
863 2020;130(3):1139-55.
864 61. Miyaoka Y, Chan AH, Judge LM, Yoo J, Huang M, Nguyen TD, et al. Isolation of single-base
865 genome-edited human iPS cells without antibiotic selection. *Nat Methods*. 2014;11(3):291-
866 3.
867 62. Barmada SJ, Skibinski G, Korb E, Rao EJ, Wu JY, and Finkbeiner S. Cytoplasmic
868 mislocalization of TDP-43 is toxic to neurons and enhanced by a mutation associated with
869 familial amyotrophic lateral sclerosis. *J Neurosci*. 2010;30(2):639-49.
870 63. Malik AM, Miguez RA, Li X, Ho YS, Feldman EL, and Barmada SJ. Matrin 3-dependent
871 neurotoxicity is modified by nucleic acid binding and nucleocytoplasmic localization. *Elife*.
872 2018;7.
873 64. Weskamp K, Safren N, Miguez R, and Barmada S. Monitoring Neuronal Survival via
874 Longitudinal Fluorescence Microscopy. *J Vis Exp*. 2019(143).
875 65. Pfaffl MW. A new mathematical model for relative quantification in real-time RT-PCR.
876 *Nucleic Acids Res*. 2001;29(9):e45.
877 66. Ishitani T, Hirao T, Suzuki M, Isoda M, Ishitani S, Harigaya K, et al. Nemo-like kinase
878 suppresses Notch signalling by interfering with formation of the Notch active
879 transcriptional complex. *Nat Cell Biol*. 2010;12(3):278-85.
880 67. Fu SC, Fung HYJ, Cağatay T, Baumhardt J, and Chook YM. Correlation of CRM1-NES affinity
881 with nuclear export activity. *Mol Biol Cell*. 2018;29(17):2037-44.
882 68. CVAT.ai, and Corporation. Computer Vision Annotation Tool (CVAT) (v2.11.2).
883 doi:10.5281/zenodo.10807509.

884 69. Cao MC, and Scotter EL. Transcriptional targets of amyotrophic lateral
885 sclerosis/frontotemporal dementia protein TDP-43 - meta-analysis and interactive
886 graphical database. *Dis Model Mech*. 2022;15(9).